UNIVERSITY OF MESSINA

DEPARTMENT OF ENGINEERING

PH.D. IN ENGINEERING AND CHEMISTRY OF MATERIALS AND CONSTRUCTION XXXIV CYCLE

ALUMINUM-BASED MATERIALS FOR THERMOCHEMICAL ENERGY STORAGE APPLICATIONS

PH.D. THESIS AUTHOR:

FABRIZIO ALVARO

TUTOR:

PROF. ELPIDA PIPEROPOULOS

CO-TUTOR:

PROF. CANDIDA MILONE

HEAD OF THE PH.D. COURSE:

PROF. GIOVANNI NERI

ACADEMIC YEARS 2018-2021

SUMMARY

ABSTRACT

The main purpose of this PhD work is the study of a new class of materials for thermal energy storage. The research for new materials for thermochemical storage (TCM), needs to develop systems based on a chemical reaction that can store/release high amounts of thermal energy, exhibit a sufficient degree of reversibility (direct and reverse reactions must occur cyclically), and ensure long-term chemical stability of reactants and products. Calcium aluminates are widely studied compounds for the production of cements. In particular, the focus has been centered on tricalcium aluminate hexahydrate ($Ca_3Al_2O_6 \cdot 6H_2O$) as a novel, low-cost, non-toxic material for energy storage applications. Such materials exhibit high heats of hydration and dehydration temperatures in the 200-350°C range, which is lower than that of more conventional materials investigated for medium temperature thermochemical storage. The development of TCMs operating at these temperatures is very limited: energy storage in the 200-300°C range is an excellent solution for the recovery of waste heat from high-temperature processes, that are the main emitters of energy at medium temperature. The work studies the material synthesis and morphological, structural and thermochemical characterization of the most thermodynamically stable compound belonging to the calcium aluminate family, the tricalcium aluminate $Ca_3Al_2O_6$.

1. INTRODUCTION

1.1 Thermal energy storage

Recent data predict that primary energy consumption will increase by 48% in 2040 [1]. Discovery of fire is considered the first milestone within the evolution of mankind, but thermal energy was readily available in nature even before human existence. Our bodies require a minimum ambient temperature to be alive. Because of that, a powerful need for thermal energy exists. Freely available solar thermal energy from sun, helps to keep up the favorable ambient thermal condition needed to sustain our lives on earth. However, the provision of radiation varies across different locations on the world, resulting in extreme cold ambient conditions within the high latitude regions to extreme hot ambient conditions near the equator. Since humans are expanding their presence across the earth into places with such extreme local conditions, need for thermal energy management arises. Moreover, our modern lifestyle has created lots of new applications for thermal energy which further increase the demand for thermal energy. Today our main user energy consumption are electricity, heat and mechanical work. International Energy Association (IEA) published the user energy consumption details as 'Final consumption'. Those energy forms like electricity, heat and mechanical work are produced from energy conversion of multiple energy sources which include both natural sources and fuel sources. IEA described the energy source details as 'Primary energy supply' [2]. In its world energy statistics, IEA report for year 2014 estimated that, world's annual 'total primary energy supply' is 573 EJ (13,699 million tons of oil equivalent) and therefore the annual 'total final consumption' is 394 EJ (9,425 million tons of oil equivalent).

During the conversion process from "Primary energy supply" to "Final consumption", a significant amount of energy (about 31%) is lost: this is directly related to dangerous consequences of the global warming like the rising sea levels because of the continuous melting of ice within the polar region. World realized the importance of renewability of energy sources during the energy crisis of the 1970s. Fuel availability is limited in supply and is non-renewable.

Therefore, it is urgent to preserve energy and to move towards clean and renewable energy sources. At the same time, the depletion of fossil resources, in addition to their negative impact on the environment has accelerated the shift towards sustainable energy sources. Renewable energies such as solar radiation, ocean waves, wind, and bio-gas play an important role in reforming the natural balance and meeting all needs [3]. The means of storing these types of renewable energy are becoming increasingly important [4]. This has brought to develop efficient and sustainable methods to store energy. Energy storage plays a crucial role in renewable energy technology systems. Thermal energy storage (TES) is a technology that stores thermal energy by heating or cooling a storage medium so that the stored energy can be used later for heating and cooling applications [5] and for power generation. Such systems are used particularly in buildings and industrial processes. The benefits of using TESs in an energy system include increased overall efficiency and improved reliability, and can lead to reductions in investment and operating costs and less pollution of the environment, i.e., less carbon dioxide (CO_2) emissions [6]. Solar thermal systems, unlike photovoltaic systems with high efficiencies, are industrially mature and use most of the sun's thermal energy during the day. However, they do not have sufficient (thermal) backup to continue operating during hours of low or no-solar radiation. TESs are becoming particularly important for storing electricity in combination with concentrating solar power (CSP) systems where solar heat can be stored for electricity generation when sunlight is not available. Storage density, in terms of the amount of energy per volume or mass unit, is important to optimize solar ratio, device efficiency, and space heating/cooling energy consumption. Therefore, it is really important to study energy storage materials in solar system applications, as they may be able to increase the energy density of small water storage tanks by reducing the solar storage volume for a given solar fraction or increasing the solar fraction for a given available volume [7]. Thermal storage on the hot and/or cold side of the system can be considered. The aforementioned allows the storage of hot water from the collectors to be supplied to the absorption chiller generator (in cooling mode) or directly to the consumers (in heating mode). The latter allows

the storage of cold water produced by the absorption chiller to be supplied inside the building. Typically, three situations are identified as "hot", "warm" and "cold" storage based on the different temperature ranges. Typically, a hot tank can work at 80-90 °C, a warm tank at 40-50 °C, and a cold tank at 7-15 °C [8]. While heat storage on the hot side of solar systems is always present, due to heating and/or domestic hot water (DHW) production, cold storage is justified in larger systems. Cold storage is used not only to gain economic benefits from lower electricity costs, depending on the time of day, but also to lower the installed cooling capacity and to allow for more continuous chiller operation [9]. The use of thermal storage initially could not provide an effective backup, consequently, thermal storage has found use in solar assisted thermal systems [10]. Since then, the study of thermal energy storage technologies has increased, leading to different results [10–15]. Most of the research has focused on only one side (cold or heat) or one component of the system or one of its integral mechanisms. For example, thermal energy storage technologies and counter approaches for the solar cooling system have been investigated [16], focusing mainly on the types of thermal accumulators used in solar cooling applications, with emphasis on temperatures greater than 100 °C. Studies have been conducted on solar collectors and thermal energy accumulators used for solar thermal applications [17]. An additional study also covered ice storage and air conditioning separately [18].

1.2 Classification and Features of Storage Systems

Due to the intermittency of availability and the constant variation of solar radiation, TES has found its place in thermodynamic systems. TES not only reduces the inequality between supply and demand by conserving energy, but also improves the thermal performance and reliability of the system. Therefore, the design of efficient and economical TES systems is of great importance. However, few solar thermal systems worldwide have employed TES on a large scale. Moreover, the design of TES systems in various domestic solar applications is currently under investigation [19]. The use of a dynamic computational fluid dynamics approach is also a widely used money-saving method, where FLUENT software is successfully used for various engineering applications [20]. The main thermal energy storage systems are shown in Figure 1. A system can be described in terms of the following characteristics [21]:

- *Capacity* defines the energy stored in the system and depends on the storage process, medium, and system size;
- *Power* defines how quickly the energy stored in the system can be discharged (and charged);
- *Efficiency* is the ratio of the energy delivered to the user to the energy required to charge the storage system. It considers the energy loss during the storage period and the charge/discharge cycle;
- *The storage period* defines how long energy is stored and lasts from hours to months (i.e., hours, days, weeks, and months for seasonal storage);
- *Charge/discharge* time defines how long it takes to charge/discharge the system; and
- *Cost* refers to the capacity (€/kWh) or power (€/kW) of the storage system and depends on the capital and operating costs of the storage equipment and its lifetime (i.e., the number of cycles).

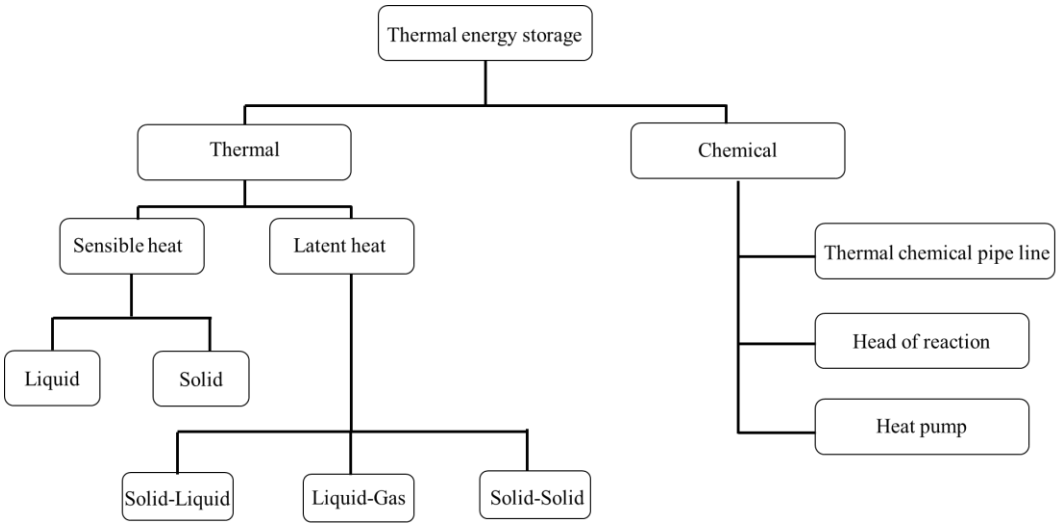

Figure 1. Types of thermal energy storage (TES).

Capacity, power, and discharge time are interdependent variables, but in some systems capacity and power may also depend on each other. The parameters for TES systems are described in Table 1 [22]. High energy storage density and high-power capacity for charging and discharging are the most desired properties of any storage system. In addition, there are three methods for TESs at temperatures from -40 °C to more than 400 °C: sensible heat, latent heat associated with PCMs, and thermochemical heat storage associated with chemistry (Figure 2) [23].

Table 1. Typical parameters of TES systems [22].

TES systems	Capacity (kWh/t)	Power (MW)	Efficiency (%)	Storage Period	Cost (€/kW)
Sensible hot water	10-50	0.001-10.0	50-90	Days/months	0.1-10
Phase-change material (PCM)	50-150	0.001-1.0	75-90	Hours/months	10-50
Chemical reaction	120-150	0.01-1.0	75-100	Hours/days	8-100

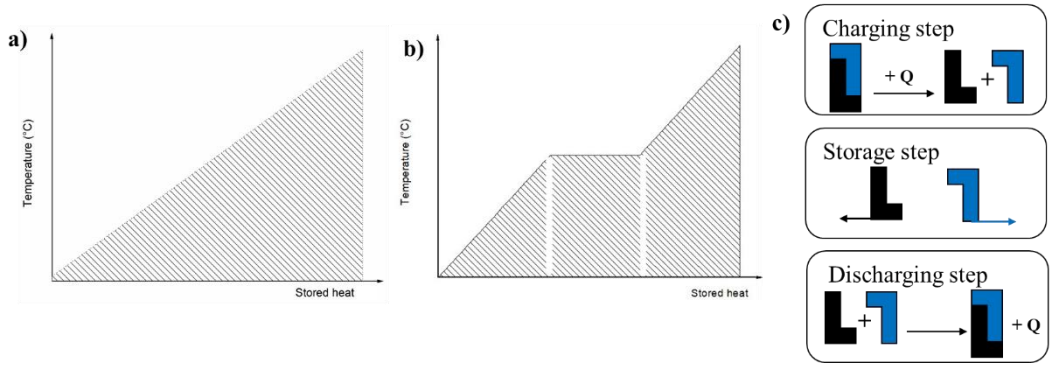

Figure 2. Methods of thermal energy storage: (a) sensible heat; (b) latent heat; (c) thermo-chemical reactions [23].

1.2.1 Sensible Heat Storage

Sensible heat storage (SHS, Figure 2a) is the simplest heat storage method based on storing thermal energy by heating or cooling a liquid or solid medium (e.g., water, sand, molten salts, or rocks), with water being the most economical alternative. Underground storage of sensible heat in both liquid and solid media is also exploited for large-scale applications. SHS has two main advantages: it is economical and no risks are associated with the use of toxic materials. SHS utilizes the heat capacity and temperature change of the storage medium during the charge and discharge process. In this case, the amount of stored heat is closely related to the specific heat of the medium, the temperature change, and the amount of storage material [24]. In sensible TES systems, energy (or heat) is stored and/or released by heating and/or cooling a liquid or solid storage material through a heat transfer interaction. The amount of energy input to a TES in a sensible heat system is related to the mass of the storage material and its heat capacity, as well as the temperature difference of the storage medium between its initial and final state. This heat transfer Q is given by the formula (Equation 1):

$$Q = mC_pT \quad (1)$$

where m and C_p represent the mass and specific heat of the storage material and T is the temperature difference before and after the storage operation. Among the

materials most commonly used as storage media, there are water, air, oil, rocks, cement, sand, and soil.

Table 2 shows the main characteristics of the most commonly used solid-state thermal storage materials [17], including sand and rock minerals, concrete, refractory bricks, and ferroalloy materials. These materials have working temperatures from 200 to 1200 °C and have significant thermal conductivities: 1.0 W/(mK)-7.0 W/(mK) for sand-rock minerals, concrete, and refractory bricks; 37.0 W/(mK)-40.0 W/(mK) for ferroalloy materials. The materials shown in Table 2 are all low cost. The major drawback is that their thermal capacities are quite low, ranging from 0.56 to 1.3 kJ/(kgC), which can make the storage unit look utopianly large.

Table 2. Solid-state sensible heat storage materials [17].

Storage Materials	**Working Temperature (°C)**	**Density (kg/m^3)**	**Thermal Conductivity (W/(m·K)**	**Specific Heat (kJ/(kg·°C)**
Sand-rock minerals	200-300	1700	1.0	1.30
Reinforced concrete	200-400	2200	1.5	0.85
Cast iron	200-400	7200	37.0	0.56
NaCl	200-500	2160	7.0	0.85
Cast steel	200-700	7800	40.0	0.60
Silica fire bricks	200-700	1820	1.5	100
Magnesia fire bricks	200-1200	3000	5.0	1.15

The most common material used in a SHS is water [8]. Hot water tanks are used for energy conservation in water heating systems through solar energy and through co-production of heat and energy. It has been shown that storage in water tanks is a cost-effective storage option and its efficiency can be further improved by

ensuring optimal stratification of water in the tank and highly effective thermal insulation [14]. The research and development focus, lately, has been on vacuum super-insulation with a thermal conductivity of 0.01 W/(mK) at 90 °C and 0.1 mbar and optimized system integration.

The energy storage capacity of a uniform temperature water (or other liquid) storage unit operating over a finite temperature difference is given by equation 2:

$$Q_s = mc_pD_{ts} \quad (2)$$

where Q_s is the total heat capacity for a cycle operating over the temperature range D_{ts}, and m and c_p are the mass and specific heat, respectively, of the water. The temperature range at which such a unit can operate is limited to the lower extreme for most applications by the requirements of the process. The upper limit may be determined by the process, liquid vapor pressure, or by the heat loss of the collector.

An energy balance on the unstratified reservoir is (equation 3):

$$mc_{Sp}\frac{dt_s}{d\tau} = Q_u - Q_L - U_s A_s (t_i - t_a) \quad (3)$$

where Q_u and Q_L are the amounts of energy addition or removal from the collector and at the load; U_s is the heat loss coefficient of the storage unit; A_s is the surface area of the storage unit; t_f is the final temperature in C; t_a is the ambient temperature of the tank; t is the time, which is used to determine the long-term performance of the storage unit and the solar process. Useful long-term analytical solutions are not possible because of the complex time dependence of some terms. There are many possible numerical integration methods. One can exploit Euler integration to predict the storage temperature of water as a function of time (equation 4):

$$t_s = t_i + \frac{\Delta\tau}{mc_p}[Q_U - Q_L - U_s A_s (t_i - t_a)] \quad (4)$$

Once the tank temperature is known, other temperature-dependent quantities can be estimated. Large hot water tanks are used for seasonal storage of solar thermal heat in conjunction with small district heating systems. These systems can have a volume of up to several thousand cubic meters. Charging temperatures are in the

range of 80-90 °C. A more complex storage system is shown in Figure 3. The so-called combistore is loaded with solar collectors and a second heating source, such as a biofuel or gas boiler, and heat is extracted through two very different mechanisms: domestic hot water and space heating [25]. The high specific heat capacity, wide availability, chemical stability, and low cost make water a good storage medium suitable for low temperature solar cooling applications. Due to the boiling point constraint (100 °C at 1 bar), the use of water as a sensible heat storage medium for high temperature applications requires the increasing of the system pressure [16].

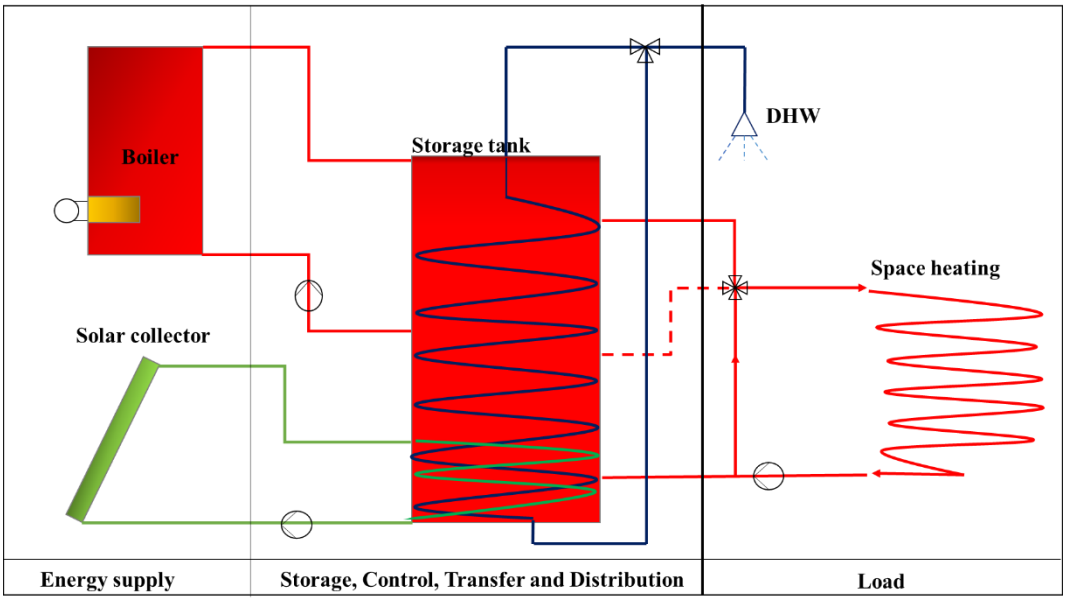

Figure 3. Schematic of a solar combisystem with solar collectors and a boiler charging water storage tank [25].

1.2.2 Latent-Heat or Phase-Change Storage

Latent-heat storage (LHS) materials are also referred to as PCMs, thanks to their ability to release or absorb energy through a physical-state change. In LHS the involved energy storage density increases. Heat is primarily stored within the physical change process, at a stable temperature, and it is directly associated with the heat energy of the material. The employment of a LHS system using PCM is an efficient method of thermal energy storage, accompanied by a high energy

storage density and including the isothermal nature of the storage process. The most advantage of using LHS than SHS is its ability to store heat at a virtually similar temperature range. At first, these materials behave like SHS materials, the temperature increases linearly with the enthalpy of the system; in a second time, heat is absorbed or released at nearly constant temperature during the physical-state change. LHS relies on the absorption or release of heat when a storage material undergoes a phase transition from solid to liquid or liquid to gas or contrariwise. The storage capacity Q_s, in J, of the LHS system with a PCM medium [17] is given by (equations 5-6):

$$Q_s = \int_{t_i}^{t_m} mc_p\,dt + mf\Delta q + \int_{t_m}^{t_f} mc_p\,dt \quad (5)$$

$$Q_s = m\left[c_{ps}(t_m + t_i) + f\Delta q + c_{pl}(t_f + t_m)\right] \quad (6)$$

where t_m is the melting temperature, in °C; m is the mass of PCM medium, in kg; c_{ps} is the typical heat energy of the solid phase between t_i and t_m, in kJ/(kg·K); c_{pl} is the common heat of the liquid phase between t_m and t_f, in J/(kg·K); f is the melt fraction; Δq is the warmth of fusion, in J/kg. To give an idea, Glauber's salt ($Na_2SO_4 \cdot 10H_2O$) has c_{ps}~950 J/(kg· °C), c_{pl} ~ 3550 J/(kg·°C), and Δq = 2.43·105 J/kg at 34 °C. The most used measurement techniques presently employed for fusion enthaply and melting temperature of PCMs are differential thermal analysis (DTA) and differential scanning calorimetry (DSC) [17]. In those techniques, sample and reference materials are heated following the same rate (or temperature program). The temperature difference between them is proportional to the difference in heat flow between the two materials and the record is the DSC curve.

As described early in Figure 1, the activity process takes place in several modes: solid–solid, liquid–gas, and solid–liquid. Within the first case, heat is stored by transition between different kinds of crystallization forms. For liquid–gas systems, heat of transformation is incredibly high, but there are problems in storage control because of the high-volume variations during state change. The most studied (and employed) materials are the solid–liquid PCMs, which have a limited volume variation during heat exchange (generally less than 10%) and a reasonably high

melting enthalpy. Melting processes involve energy densities of 100 kWh/m^3 (e.g., ice) compared to a typical 25 kWh/m^3 for SHS options. PCMs may be used for both short-term (daily) and long-term (seasonal) energy storage, employing a form of techniques and materials.

The possible uses of PCMs are as follows:

- implementation in wall cladding materials that are a part of the building structure to boost thermal energy storage capacity, with main use in peak load transfer and solar power [26]; during this case, the standard operating temperature is 22-25 °C, but may vary counting on climate and heating/cooling loads;
- cold storage for cooling systems (operating temperature 7-15 °C)[27];
- hot storage for heating systems (40-50 °C) [27];
- hot storage for solar cooling and heating (80-90 °C) [27].

Thus, any latent thermal energy storage system has the subsequent three components by default:

a. a PCM having as its freezing point the one required for the temperature range,
b. an acceptable heat transfer surface,
c. a container compatible with the PCM

PCMs have been used in thermal applications for several decades. PCMs exhibit advantageous thermophysical, kinetic and chemical properties, as well as economic advantages. LHS materials are classified based on their physical transformation for heat absorption and desorption capabilities. As shown in Figure 4, there are classifications of solid-liquid PCMs, which are in turn classified into organic, inorganic, and eutectic materials.

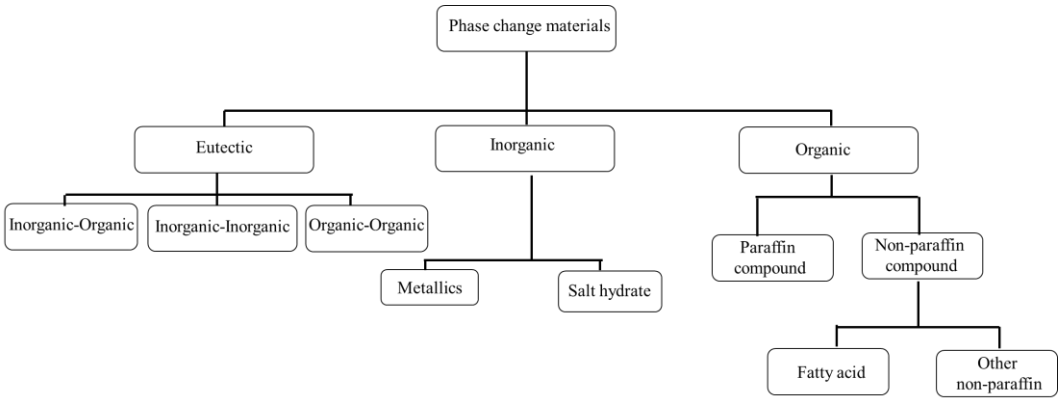

Figure 4. Classification of phase-change materials (PCMs) [15].

PCMs are classified into different groups depending on the nature of the material (kerosene, fatty acids, salt hydrates, etc.). The advantages and disadvantages of organic and inorganic PCMs are shown in Table 3 [28].

Table 3. Comparison of organic and inorganic materials for heat storage [28].

Organic	**Effect on Solar Cooling System**	**Inorganic**	**Effect on Solar Cooling System**
Advantages		***Advantages***	
Non corrosive	good	Greater phase change enthalpy	good
Low or no undercooling	crucial		
Chemical and thermal stability	important		
Disadvantages		***Disadvantages***	
Lower phase change enthalpy	bad	Subcooling	crucial
Low thermal conductivity	crucial	Corrosion	undesirable
Inflammability	undesirable	Phase separation	undesirable
		Lack of thermal stability	crucial

Considering real applications in thermal energy store, paraffins (organics), hydrated salts (inorganic), and fatty acids (organics) are the most considered materials. For cold storage applications, water is commonly used as well.

Table 4 exposes some relevant PCMs covering a wide temperature range. Melting temperature, enthalpy, and density are reported. An ingenuous composite PCM of caprylic-nonanoic acid and expanded graphite (CA-NA/EG) with an optimum absorption ratio (CA-NA/EG = 90:10, by mass) was prepared by Wang et al. [29]. The composite PCM has no supercooling, proper temperature, acceptable heat and thermal conductivity, and excellent thermal reliability and stability.

Table 4. Some relevant PCMs properties**.**

PCM	Melting Temperature (°C)	Melting Enthalphy (kJ/kg)	Density (g/cm^3)
Ice	0	333	0.92
Na-acetate thrihidrate	58	250	1.30
Paraffin	-5-120	150-240	0.77
Erytriol	118	340	1.30

Optimal handling and appropriate systems are required using PCMs to mantain the material in liquid and solid phase and to prevent its possible variation in chemical composition by interaction with the surrounding atmosphere, to extend its compatibility with other materials inside the storage system and to provide an adequate surface for heat transfer. A large variety of systems has been already studied for bulk storage in tank heat exchangers, macro-encapsulation, and micro-encapsulation. The principal advantage of PCM bulk systems is the higher storage density than that found in non-PCM, which means more efficiency or/and lower space required to implement that kind of technology. Extensively used approaches involve inserting fins and using high conductivity particles, metal structures, fibers on the PCM side, direct contact heat exchangers or the rotating cylinder method [30].

The two other possibilities are macro- and micro-encapsulating [31]. Macro-encapsulating, which is the most used, consists in including a PCM in an exceedingly tube, sphere, panel, cylinder, etc. The choice of the encapsulation material (plastic or metallic-aluminum or steel) and also the geometry affects the thermal performance of the storage. Micro-encapsulating consists in small sphere (diameter < 1 mm) of PCM encapsulated by means of a very thin and high molecular weight polymer. The spheres are then incorporated in some compatible material. The developed capsule is utilized in one-tank TES system as shown in Figure 8. Heat is then transferred to or from a heat transfer fluid, because the heat transfer fluid flows through the space between the capsules. During the charging mode, the new fluid is circulated through the tank. The PCM inside the capsules absorbs heat of transformation and melts. During the discharging mode, cooler heat transfer fluid is circulated through the tank to soak up heat from the PCM, causing the encapsulated PCM to freeze.

PCM encapsulation has been used extensively in building cooling systems where PCM are positioned in flat containers [32]. The effect of encapsulated PCM incorporates a good scope in enhancing the performance of LHS systems [33] employed in the solar absorption cooling system. Organic PCMs are often encapsulated physic-mechanically, chemically, and physic-chemically. Various approaches to organize the encapsulated PCM (organic) as a reasonably TES medium replacement are extensively developed and might be manufactured to suit the required properties [34].

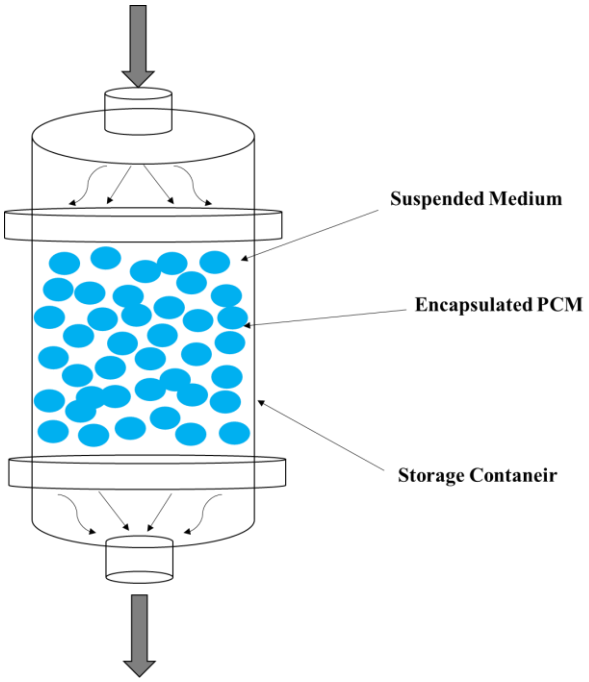

Figure 5. Direct contact TES system [32].

The main advantages of PCM versus water SHS are [10]:

- the likelihood of reducing the tank volume for a given amount of energy stored, which may be done providing that the storage is operated during a very narrow temperature range round the phase-transition temperature, and
- fewer on–off cycles of auxiliary heaters (for plants with storage on the hot side) and chillers (for plants with storage on the cold side).

The main disadvantages of PCM versus water SHSs are [10]:

- higher investment costs, and
- higher risks, due to leaks of stability and erosion of fabric encapsulating PCMs.

These materials make use of the heat energy between the solid- and liquid-phase change and must be encapsulated or stabilized for technical use in any building system, active or passive. This could be achieved via direct inclusion within the wall, by impregnation during a porous material like gypsum [35], via micro-encapsulation techniques [36], or by employing a shape-stabilization or slurries of

PCM suspended on a thermal fluid [37]. Encapsulation may be a key issue for the implementation of those technologies in buildings and must be designed to avoid leakage and corrosion. Material selection and LHS design are the most significant steps. PCM is chosen based upon its melting temperature and warmth of fusion. The parameters necessary to spot the fabric include the temperature required for the appliance and warmth requirements. Thus, the sort of PCM is chosen for its physical and chemical properties, considering the drawbacks. Heat flux DSC is one amongst the foremost reliable methods of laboratory thermal analysis for testing heat storage capacity of PCM with a relentless heating/cooling rate [38]. A visual combination of important thermal properties (Figure 6) of some kinds of PCM was produced by Li et al. [39].

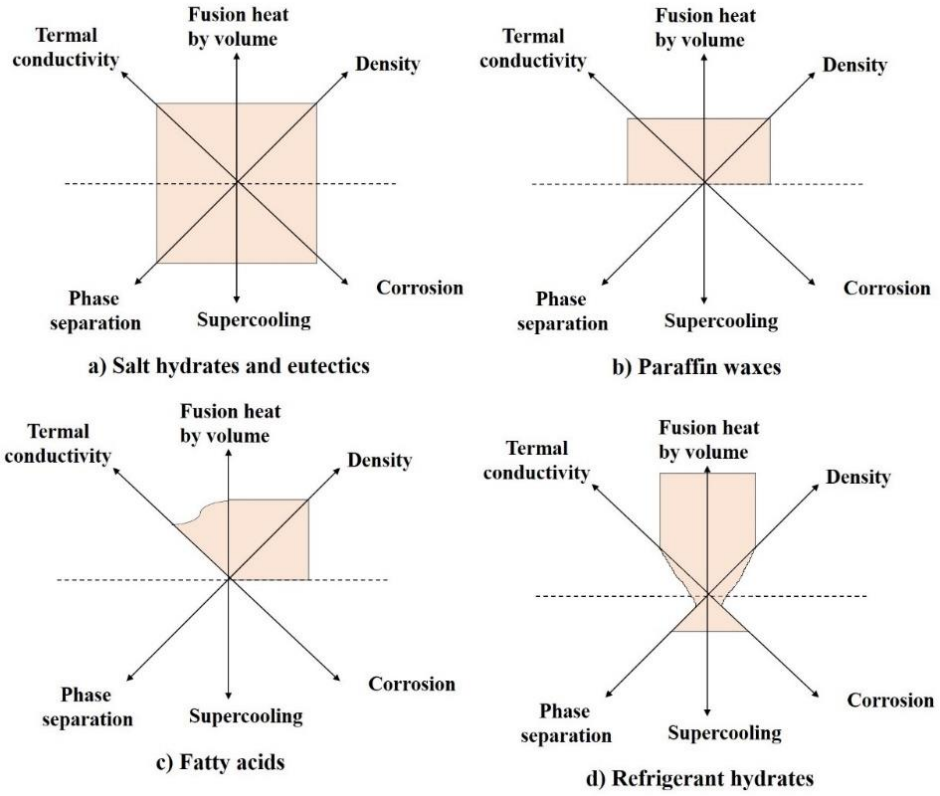

Figure 6. Thermal properties of various PCMs [39].

1.2.3 Thermochemical Energy Storage

Thermochemical energy storage (TCES) category includes sorption and thermochemical reactions. In TCES, energy is generally stored after a decomposition reaction and so recovered by the reverse reaction.

Thermochemical energy storage shows higher storage density than the opposite sorts of TES, allowing large quantities of energy to be stored using small amounts of storage material. Energy storage supported by chemical reactions is especially appropriate for long-term storage applications, e.g., seasonal storage of solar heat, because the method involves almost no energy losses during the storing period. Storage is sometimes carried out at ambient temperatures. Sorption systems (adsorption and absorption) are chemical processes involving intermolecular forces and thus are considered chemical heat storage. Adsorption occurs when an adsorptive accumulates on the surface of an adsorbent and shapes a molecular or atomic layer. The adsorptive is often liquid or gas while the adsorbent is often solid or liquid. Absorption could be a process that happens when a substance is distributed into a liquid or solid and forms an interaction.

TCES uses thermo-chemical materials (TCM), which store and release heat by a reversible endothermic/exothermic reaction process (Figure 2c). During the charging process, heat is applied to a reactant, leading to a separation of two or more components (products). The resulting reaction products will be easily separated and stored until the discharge process is required. Then, the previously formed products are mixed at suitable pressure and temperature conditions, and energy is released as a consequence of the reverse reaction occurs. The products are often stored separately, and thermal losses from the storage units are restricted to sensible heat effects, which are usually small compared to the energy of reaction. Thermal decomposition of metal oxides for energy storage has been widely considered [40]. These reactions can have an advantage based on the fact that the developed oxygen is often used for other purposes and oxygen from the atmosphere will be used in the reverse reactions. Two examples include the

decomposition of potassium oxide (equation 7), which occurs in a temperature range of 300–800 °C with a heat of decomposition of 2.1 MJ/kg, or lead (IV) oxide (equation 8) which occurs in a temperature range of 300–350°C with a heat of decomposition of 0.26 MJ/kg.

$$4KO_{2(s)} \rightleftharpoons 2K_2O_{(s)} + 3O_{2(g)} \quad (7)$$

$$2PbO_{2(s)} \rightleftharpoons 2PbO_{(s)} + O_{2(g)} \quad (8)$$

However, there are many practical and technical problems yet to be faced within the use of those reactions. Energy storage by thermal decomposition of calcium hydroxide, $Ca(OH)_2$, has been extensively studied by Fujii et al. [41]. The reaction is (equation 9):

$$Ca(OH)_{2(s)} \rightleftharpoons CaO_{(s)} + O_{2(g)} \quad (9)$$

The decomposition reaction will proceed at temperatures above ~450 °C; the rates of reaction may be enhanced by doping with zinc or aluminum the crystal structure of calcium hydroxide. Calcium oxide is stored under anhydrous conditions to avoid back-reactions occurring before it is necessary. Then, when water vapour is mixed with CaO, the reverse reaction proceeds easily.

An example of a photochemical reaction is the decomposition of nitrosyl chloride, NOCl, which might be written as a double step (equations 10-11):

$$NOCl_{(g)} + h\nu \rightleftharpoons NO\cdot + Cl\cdot \quad (10)$$

$$2NOCl_{(g)} + h\nu \rightleftharpoons 2NO\cdot + Cl_{2(g)} \quad (11)$$

Radiation at precise wavelength and frequency causes the homolytic scission of nitrosyl chloride into nitrogen monoxide and atomic chlorine (10). The produced atomic radical chlorine forms chlorine gas immediately, Cl_2, with the discharge of a considerable part of the energy, added to the NOCl, in decomposition (11).

Thermochemical reactions are often suitable to store heat and cold, in addition to the humidity control. The high storage capacity of sorption processes also allows thermal energy transportation.

Table 5 lists some of the most interesting chemical reactions for TES [42], classified for type of process. While physical sorption storage can only work on temperatures up to ~350 °C, temperatures of chemical reactions can go much higher.

Table 5. Some chemical reactions for thermal energy storage [42].

Reaction	Equation	T range (°C)	Energy Density (kJ/kg)
Methane steam reforming	$CH_4 + H_2O \rightleftarrows CO + 3H_2$	480-1195	6053
Ammonia dissociation	$2NH_3 \rightleftarrows N_2 + 3H_2$	400-500	3940
Thermal dehydrogenation of metal hydrides	$MgH_2 \rightleftarrows Mg + H_2$	200-500	3079 (heat) 9000 (H_2)
Dehydration of metal hydroxides	$Ca(OH)_2 \rightleftarrows CaO + H_2O$	402-572	1415
Catalityc dissociation	$SO_3 \rightleftarrows SO_2 + \frac{1}{2} O_2$	520-960	1235

During the thermochemical storage reaction, expressible as (equation 12):

$$A + \text{heat} \rightleftharpoons B + C \qquad (12)$$

A is the thermochemical material (TCM) for the reaction. It could be a hydroxide, hydrate, carbonate, ammoniate, etc. Usually, products B and C have different physical state, making the separation process easier to be carried out.

In general, a TES cycle includes three main processes:

I. Charging
II. Storing
III. Discharging

These three processes are illustrated for thermochemical energy storage in Fig. (2c), and are described individually as below:

- *Charging*

The charging process is endothermic. Thermal energy is absorbed from an energy source, which may be a renewable energy resource and/or conventional energy sources like fossil fuels. This energy is employed for dissociation of the thermochemical material. Of course, to let the reaction occur completely, energy should be comparable to reaction enthalpy ($Q \sim \Delta_r H$).

- *Storing*

After the charging process, components B and C are separately stored with few or no energy losses. The materials are usually stored at ambient temperatures, leading to no thermal losses (except during the initial cooling after charging). Unexpected energy losses may be possible due to degradation of the materials.

- *Discharging*

During this process, B and C are combined together again. The energy released by this reaction allows the stored energy to be recovered. After discharging, starting material A is regenerated and could be used again in a next cycle.

1.3 Assessment and comparison of thermochemical TES systems

Thermochemical TES is assessed and compared to other varieties of TES, considering thermochemical material candidates, factors affecting their selection and first advantages. Thermochemical TES systems have several advantages over other kinds of TES:

- Components (B and C) can usually be stored separately at ambient temperature, after their formation, cooling to ambient conditions. Therefore, there is a neglectable heat loss during the storing period and, as a consequence, insulation is not needed.
- As a result of the low heat losses, thermochemical TES systems are especially suitable for long-term energy storage (e.g., seasonal storage).
- Thermochemical materials have higher energy densities relative to PCMs and sensible storage media. Thanks to higher energy density, thermochemical TES systems can provide more compact energy storage in comparison to latent and sensible TES. This attribute is particularly beneficial where the volume for TES material is proscribed or valuable.

Key parameters for the selection of a thermochemical material, shall include:

- ✓ Low costs
- ✓ Cyclic behavior, meaning reversibility and low degradation over a significant number of cycles
- ✓ Availability
- ✓ Toxicity and safeness
- ✓ Corrodibility
- ✓ Energy storage density
- ✓ Reaction temperature
- ✓ Reaction rate
- ✓ Ability to be engineered into a practical system

The basic theory of thermal energy storage and conversion by chemical action will be found in [43,44]. Over the last 20 years, the experimental research on chemical reactions has been focused on the hydration and carbonation of metal oxides. These

reactions are generally useful to store medium and high-temperature heat (>400 °C). The reaction enthalpy for those reactions are typically within the range from 80 to 180 $kJmol^{-1}$. As within the case of sorption processes, the main drawbacks in solid–gas chemical reactions are the poor heat and mass transfer performance in their active bed and therefore the low thermodynamic efficiency of the cycle (reactor temperature swing), which is critical for continuous operation. So far, the research direction on chemical process heat pumps has been focused on improving the performance of the system by applying composite materials to the planning of the reactor and heat exchanger.

Kato et al. [45] developed a chemical apparatus for the dehydration and hydration of $Mg(OH)_2$/MgO. The chemical setup is meant to recover waste heat from the exhaust gas of combustion engines (gas and diesel, like cogeneration systems, vehicles, fuel cells, micro-gas turbines, etc.) at around 250–400 °C and to provide heat at around 100–250 °C with a water vapour pressure below 400 kPa [46]. The reactants employed in the experiments were MgO made of ultra-fine particles with high purity and pure water. Studies [47–49] showed that MgO had great reactivity and high durability to repetitive reaction cycles. Again Kato et al. [50] obtained a mean heating power of 119 W kg_{salt}^{-1} during the initial 60 min, when the operating temperatures were 400 °C/30–200 °C/121 °C. in an exceedingly later study [46], a carbon fiber sheet fin was used for thermal conductivity enhancement within the packed bed. The reported mean heating power was 49 W kg_{salt}^{-1} at temperatures of 150–160 °C during the initial 100 min, when the initial bed temperature was 120 °C, the evaporator temperature was 85 °C and also the $Mg(OH)_2$ was previously dehydrated at 430 °C. Kato et al. [51] and Ryu et al. [52] also showed that when the $Mg(OH)_2$ was mixed with $Ni(OH)_2$ or $Co(OH)_2$ at atomic level, the new material was ready to store heat at lower temperatures (200–300 °C), at which pure $Mg(OH)_2$ could not be dehydrated. However, several issues related to their material were found. Further research was administrated by Kim et al. [53] and Mastronardo et al. [54–57] on magnesium hydroxide hybrid materials with carbon (expanded graphite, carbon nanotubes, functionalized carbon nanotubes) to boost the thermal conductivity and

reactivity of magnesium oxide/water chemical setup. Additionally, salt was also introduced into the mixture of expanded graphite and $Mg(OH)_2$ to make sure smooth diffusion of vapor in materials and enhance fit ability between expanded graphite and $Mg(OH)_2$. The composite materials showed a better reactivity than pure $Mg(OH)_2$.

Ogura and Mujumdar [58] proposed a chemical setup dryer (CHPD) supporting the hydration and dehydration of CaO/ $Ca(OH)_2$. The proposed CHPD consists of two chemical heat pumps (CHP), both supporting the identical action. The pumps produced hot air for the drying room by using the heat released from the reaction or from the condensation of water (Fig. 7). The two CHPs operate concurrently within the heat enhancement mode. CHP1 is within the heat storage step (charging, T_h >594 °C and T_m ≅150 °C), while CHP2 is within the heat release step (discharging, T_m¼ 360 °C and T_l¼ 20 °C). After every hour approximately, the two heat pumps swap operating steps.

Ogura et al. [59] experimentally evaluated the performance of the chemical apparatus for the hydration reaction, i.e. CHP2 in Fig. 7. The experiments were performed during a multi-tray packed bed reactor and each tray had radial fins for heat transfer enhancement. At the evaporation temperature of 20 °C and initial air temperature of 27 °C, the outlet air temperature from the heat exchanger quickly achieved a maximum temperature of 187 °C, decreasing gradually to 47 °C after 600 min. The reported average heating power was 2.86 kW (477 $W \cdot kg_{salt}^{-1}$) for 30 min operation while 1.77 kW (295 $W \cdot kg_{salt}^{-1}$) for 60 min operation. Further studies were focused on the controllability of the output characteristics of the CHP. The experiments were administrated at different operating temperatures for the heat storing step (T_h¼ 550–770 °C and T_m¼ 77 °C) and for the heat releasing step (T_l¼ 5–20 °C), within the heat storage step. It was found that heat at 77 °C is generated within the condenser even when the dehydration temperature is as low as 550 °C (30% of conversion after 170 min). On the other hand, during the heat release, heat at above 127 °C was generated within the reactor even when the evaporator temperature was at 5 °C. Finally, it was concluded that the CHP is also controlled by operating temperature and pressure control of the chemical reactions.

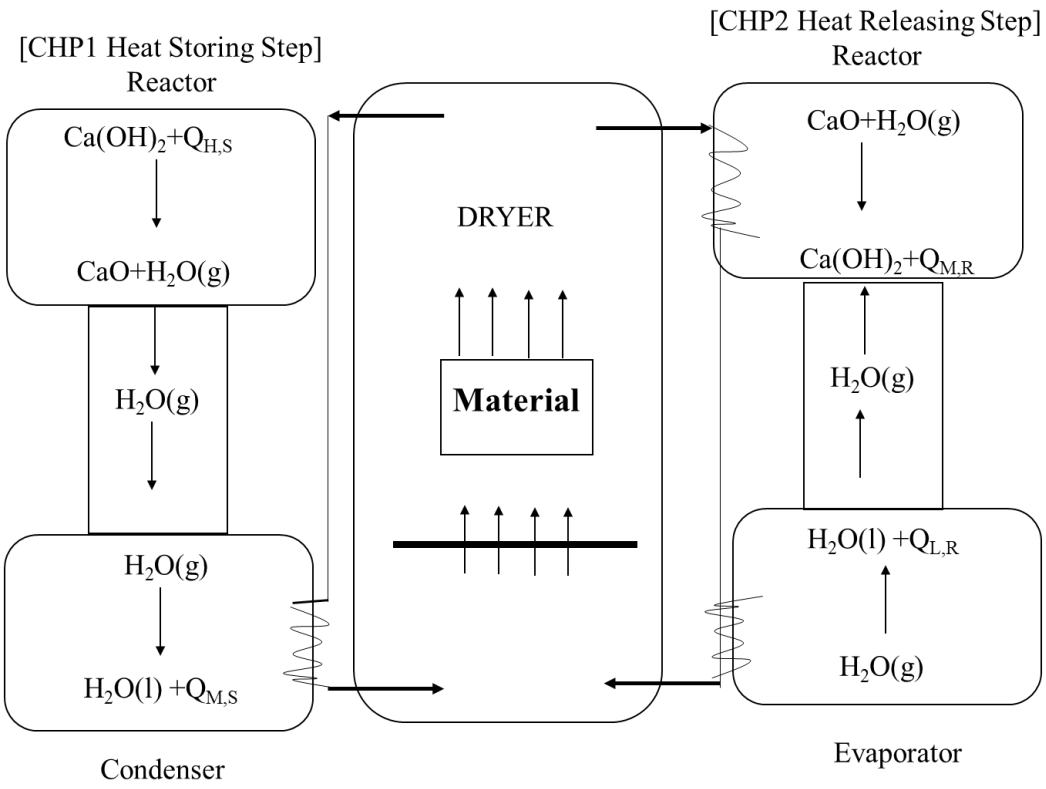

Figure 7. Schematic diagram of the $CaO/H_2O/Ca(OH)_2$ CHPD system [58].

Cerkvenik et al. [60] tested a refrigeration chemical setup based also on the reversible hydration of CaO, which was combined with expanded graphite by a suspension method. The mixture was then dried and pressed into the required form. To increase the mass transfer of the reactive block, three vapor channels were made within the graphite matrix. The common SCP was about 50 kWh when the cycle time was limited to 1000 s (70 % of conversion) at the pressure level of 0.75 kPa (typical value for refrigeration) and hydration temperature of 200 °C. Moreover, the effect of three vapor channels was compared with a study administrated by Depta [61] where only one vapor channel was used. At the hydration temperature of 200 °C with a vapour pressure of 1.5 kPa, the authors found that the cycle time with three vapor channels was about four times longer than that with one vapor channel.

Kato et al. [60–62] also developed a double reactor variety of heat transformer, supporting the reversible carbonation of lime (CaO) and lead (II) oxide (PbO) via greenhouse emission (CO_2). This chemical setup was developed

to store heat within the CaO reactor from an extreme temperature process (e.g. 4860 °C) and upgrade it to higher temperatures (e.g. 4900 °C) for a turbine generator. Additionally, the energy released during heat storing step from the carbonation of PbO may well be used as heat source of a steam-turbine. The authors obtained a mean heating power of 238 Wkg_{salt}^{-1} at temperatures of 900–990 °C during the initial 60 min of the heat releasing step, when the cycle was conducted under isothermal conditions at a pressure of 30.4 kPa and 304 kPa, respectively during dehydration, and hydration .

1.4 Materials for thermochemical storage (TCM) - Calcium Aluminates

Regarding the type of use, the research focuses on new materials or possible precursors with low costs and high availability, as well as compatibility with the project that foresees a future use. Once a suitable material has been chosen, it is necessary to consider and investigate important aspects such as:

- Storage capacity;
- Thermal transmission efficiency;
- Long-term mechanical and chemical durability with respect to thermal charge/discharge cycles;
- High conversion rate in charge/discharge cycles;
- Small heat losses;
- Ease of control;
- Sufficient maximum load;
- Suitable operating temperature for the application (low, medium, high);
- Specific enthalpy drops during loading.

Materials for thermochemical storage, currently being studied or already used in some cases, include different inorganic compounds, as shown in Table 6 [63].

Table 6. Materials of main interest in the field of TCES [63].

Material	**Reaction products**		**Reaction onset temperature**	**Storage density**
Formula	**Solid**	**Gas**	**T_{onset} (°C)**	**Q_s^V (GJ/m^3)**
$MgSO_4 \cdot 7H_2O$	$MgSO_4$	H_2O	122	3.3
$CaSO_4 \cdot 2H_2O$	$CaSO_4$	H_2O	89	1.4
$Al_2(SO_4)_3 \cdot 6H_2O$	$Al_2(SO_4)_3$	H_2O	150	1.9
$Li_2SO_4 \cdot H_2O$	Li_2SO_4	H_2O	103	0.9
$CuSO_4 \cdot 5H_2O$	$CuSO_4$	H_2O	92	2.1
$FeCO_3$	FeO	CO_2	180	2.6
$CaCl_2 \cdot 2H_2O$	$CaCl_2$	H_2O	95	1.1
$MgCl_2 \cdot 6H_2O$	$MgCl_2$	H_2O	150	2.5
$Na_2S \cdot 5H_2O$	Na_2S	H_2O	80	3.6
$Mg(OH)_2$	MgO	H_2O	332	2.8
$Ca(OH)_2$	CaO	H_2O	512	2.9

In the research for new materials for thermochemical storage (TCM) in the medium temperature range (100°C/350°C), the focus has been centered on those materials that increase their internal energy, and thus temperature, by absorbing thermal energy. The materials of interest are calcium aluminates (Table 7). These compounds that normally find use in building applications, i.e., cement technology, are now being studied as thermochemical storage materials.

Table 7. Most common Calcium Aluminates.

Formula	**Systematic name**
$Ca_3Al_2O_6$	Tricalcium aluminate
$Ca_{12}Al_{14}O_{33}$	Dodecacalcium heptaaluminate
$CaAl_2O_4$	Calcium aluminate

$CaAl_4O_7$	Calcium dialuminate
$CaAl_{12}O_{19}$	Calcium hexaaluminate
$Ca_2Al_2O_5$	Dicalcium aluminate
$Ca_5Al_6O_{14}$	Pentacalcium trialuminate
$Ca_4Al_6O_{13}$	Tetracalcium trialuminate

The choice to study this family of compounds for Thermochemical Energy Storage (TCES) derives from some interesting characteristics such as high heats of hydration and dehydration temperatures in the range 200°C-350°C, lower than the more conventional materials investigated for medium temperature thermochemical storage. In cement technology, these compounds (*CAC - Calcium Aluminate Cements*) release high amounts of heat when mixed with water [64]. For this reason, an interest arose to know in detail the processes and chemical species involved during the hydration reaction of calcium aluminate cements.

According to recent studies, the great amount of heat of hydration is released when tricalcium aluminate ($Ca_3Al_2O_6$) is hydrated to the formation of a hexahydrate species, as shown below in equation 13:

$$Ca_3Al_2O_{6\,(s)} + 6H_2O_{\,(l)} \rightarrow Ca_3Al_2O_6{\cdot}6H_2O_{\,(s)} \qquad (13)$$

The standard reaction enthalpy for eq. 13 is $\Delta H° = -258.6$ kJ/mol [65,66]. Therefore, considering both the high heat involved and the density of the compound (~ 3 kg/dm^3), the theoretical storage density would be higher than 2800 $\frac{MJ}{dm^3}$. Tricalcium aluminate hexahydrate, $Ca_3Al_2O_6{\cdot}6H_2O$, known as katoite mineral, belongs to the hydrogarnet group [67]. Studies on thermal decomposition, reported a two-step process in which the first dehydration takes place at 240–300 °C and the 1.5-hydrate product is formed [68]. Of course, the temperature is affected by many factors such as crystallinity, structural phase and additives. The reaction is reversible; indeed, $Ca_3Al_2O_6{\cdot}1.5H_2O$ is used as drying agent due to the high tendency to adsorb water vapor from the surrounding atmosphere (Equation (14)) [69]. At higher temperature (> 550 °C) $Ca_3Al_2O_6{\cdot}1.5H_2O$ transforms into mayenite ($Ca_{12}Al_{14}O_{33}$) [70].

$Ca3Al2O_6 \cdot 6H_2O_{(s)} \rightleftarrows Ca_3Al_2O_6 \cdot 1.5H_2O_{(s)} + 4.5H_2O_{(g)}$ (14)

Then, taking into account the promising features of $Ca_3Al_2O_6$, an attempt was made to assess it for possible application in the field of TES.

1.5 Outline

The path followed during the development of this research work is briefly discussed below. The first step of the study on new materials for thermochemical storage involved an accurate bibliographic research, in order to clarify the current state of the art of this technology and, at the same time, to highlight potential lack in the development of this type of materials, taking into account working temperature, storage capacity (energy per mass unit), storage density (energy per volume unit), durability (number of effective cycles before replacement or restoration of the material), application conditions. Once the operating temperature range of 200-350 °C was highlighted as the most deficient in the thermochemical field, attention was paid to potential candidate materials. The choice was made on the basis of specific characteristics (cost and availability of materials or precursors, standard enthalpy of reaction, thermal stability). The approach to the experimental work was therefore to first look for materials available on the market that could already meet the essential requirements as TCM, at the same time, easily achievable synthesis methods were studied. The characterization of the studied materials, both thermochemical (TGA, DSC) and structural (XRD) and morphological (SEM, DLS, BET), played a primary role in the feasibility of the work and in clarifying many aspects on the behavior of these systems. The simulations of the working conditions of a chemical heat pump, using an appropriate thermogravimetric system, allowed to have the first results on the studied samples, which proved to be promising. More in-depth work was carried out on the most performing material, composed of tricalcium aluminate hexahydrate, to better clarify the thermodynamic and kinetic aspects. At the same time, attempts at alternative syntheses aimed at increasing the characteristics of the material have been conducted. This type of study, which is still under construction, will be described in the last part of the work.

2. EXPERIMENTAL CHAPTER

In this chapter, the main results obtained during this PhD course will be discussed.

Some of these studies, which will be discussed in the next paragraphs, led to the following publication in an international journal:

- ✓ Alvaro, F.; Piperopoulos, E.; Calabrese, L.; La Mazza, E.; Lanza, M.; Milone, C. Performances Assessment of Tricalcium Aluminate as an Innovative Material for Thermal Energy Storage Applications. *Appl. Sci.* 2021, *11*, 1958. https://doi.org/10.3390/app11041958

In the study of a material for a future application in energy storage, the main used techniques concern, first of all, the morphological and structural characterization, in addition to the determination of the thermochemical behavior.

Thermochemical behavior:

- Thermogravimetric analysis (TGA)
- Differential scanning calorimetry (DSC)

Morphological and structural characterization:

- Scanning electron microscopy (SEM)
- X-Ray Diffraction (XRD)

The investigation of tricalcium aluminate was conducted starting from the synthesis of the material, and then performing the structural characterization, as well as the determination of the thermochemical behavior, with the aim of evaluating the cyclability of the dehydration-hydration reactions and the heat involved during these processes.

2.1 Instrumental techniques

In this section the main instrumental techniques used to study the material are discussed, they will cover both the structural study (XRD, SEM) and the study of thermochemical properties (DSC, TGA).

2.1.1 X-Ray Diffractometry (XRD)

This technique [71] is mainly used to identify the structural characteristics of a solid-state material. The working principle of this technique is based on the interaction between a beam of monochromatic X-rays and a sample (single crystal or powder), allowing to measure the diffraction angles and to correlate them to the solid structure itself. Thus, through XRD is possible to define: size and geometry of a unit cell, based on the angular values of the diffraction peaks; arrangement of the atoms within the elementary cell, by measuring the relative intensities of the peaks. A diffractometer, as schematized in Figure 8, consists of:

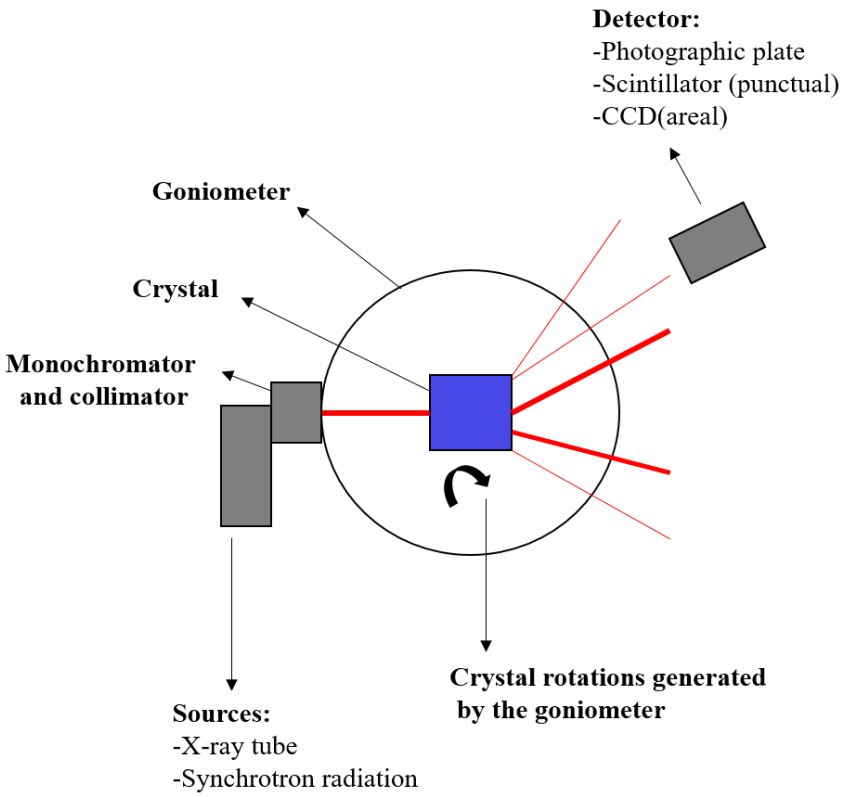

Figure 8. Schematization of X-ray diffractometer.

- A source: where an X-ray tube provides the radiation that will be directed to the sample. The emitted radiation is due to the impact of a beam of electrons against a metal anode (tungsten filament). The X-ray beam is monochromatic by means of filters of a suitable metal;
- Goniometer: to mechanically couple the carriage and the sample, so that a rotation of θ degrees of the sample corresponds to a rotation of 2θ degrees of the detector. In this way, the angles of incidence and reflection are kept equal to each other;
- Detector: main component of this instrumentation as it allows the measurement of the intensity of diffracted radiation. The diffracted beams, generated by the impact of the monochromatic beam on the particles of the solid, are intercepted by the detector that, moving at a constant angular velocity, allows a recorder to automatically draw the graph of the intensity of the diffracted beam as a function of 2θ, angle of diffraction obtained experimentally.

2.1.2 Scanning Electron Microscopy (SEM)

As suggested by the name, this microscope uses a focused beam of electrons for imaging in a similar way a photon beam does in optical microscopy. The resolution of these instruments depends mainly on the wavelength of the particle used as probe: from a comparison between the wavelengths of photons and electrons, the resolution of the electron microscope is higher than that of the optical microscope of about 1000 times.

There are two types of electron microscopes:

- ✓ The transmission electron microscope (TEM), which reveals electrons passing through a very thin sample thickness, providing two-dimensional images;
- ✓ The scanning electron microscope (SEM), which uses electrons that are repelled from the near-surface area of the sample to generate the image.

In the study of powder samples, such as those analyzed during this work, the use of the scanning electron microscope is more useful because this allows three-dimensional imaging.

The main components of the SEM are (Figure 9):

- Illumination source
- High vacuum system
- Electromagnetic lenses
- Deflection coils
- Objective lens
- Signal detectors
- Signal transformation system into images
- Sample chamber

Initially, a high-energy electron beam is generated in vacuum, focused by a lens system and deflected to scan an area of the sample. The beam-sample interaction generates various signals that are acquired by appropriate detectors and subsequently processed to form a gray-scale image. The beam is generated at the top of a column and emitted when the thermal energy of the electrons exceeds the emission energy of the source material (usually tungsten).

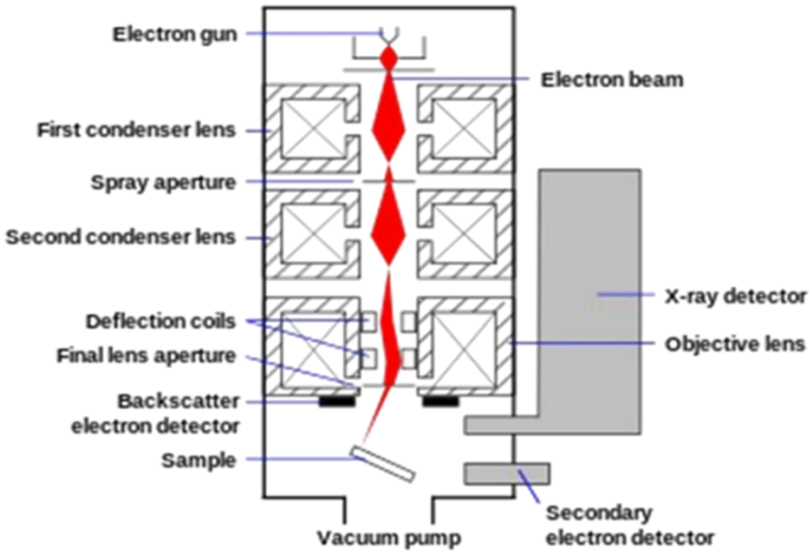

Figure 9. Cross-sectional representation of the SEM column.

The entire system is sealed in a chamber to preserve the vacuum and protect it from contamination, vibration or noise. The vacuum is useful in order to:

- obtaining high resolution images, due to the absence of interfering molecules or atoms between beam and sample;

- increasing the detectors performances to collect the generated signals (backscattered electrons, secondary electrons and X-rays).

Electromagnetic lenses are critical for electron beam control, these simply consist of a coil of wires within magnetic poles. Electron microscopes are constantly improving and new applications are arising all the time, making these instruments fascinating and with many capabilities yet to be discovered.

2.1.3 Differential Scanning Calorimetry (DSC)

Differential Scanning Calorimetry, DSC [72] (Figure 10), is considered the principal analysis technique to derive information about a material (polymeric, metallic or ceramic) when it is subjected to a heat treatment. In particular, Differential Scanning Calorimetry bases its measurements on the difference in the amount of energy (absorbed or released) between the sample under examination and a reference material, subjected to the same temperature program. Through DSC analysis it is possible to perform a large number of experiments i.e. thermal stability tests or study a huge variety of kinetics (crystallization, decomposition, absorption-desorption).

Figure 10. DSC Instrument.

This technique is advantageous for a number of reasons such as:

- Small amounts of sample required;
- Non-destructive process, unless the thermal degradation threshold of the material is exceeded;
- It is exploited to specify the reversibility of a given phenomenon following successive thermal cycles;
- It is useful for analyzing aging phenomena through appropriate heat treatments.

The information that can be deduced from a DSC measurement are (Figure 11):

- ✓ The temperature range within which a thermal process occurs and the attached peak temperature (corresponding to the minimum or maximum point of the peak, depending on the endo or exotherm of the process).
- ✓ The heat involved, which can be calculated from the integral of the peak.

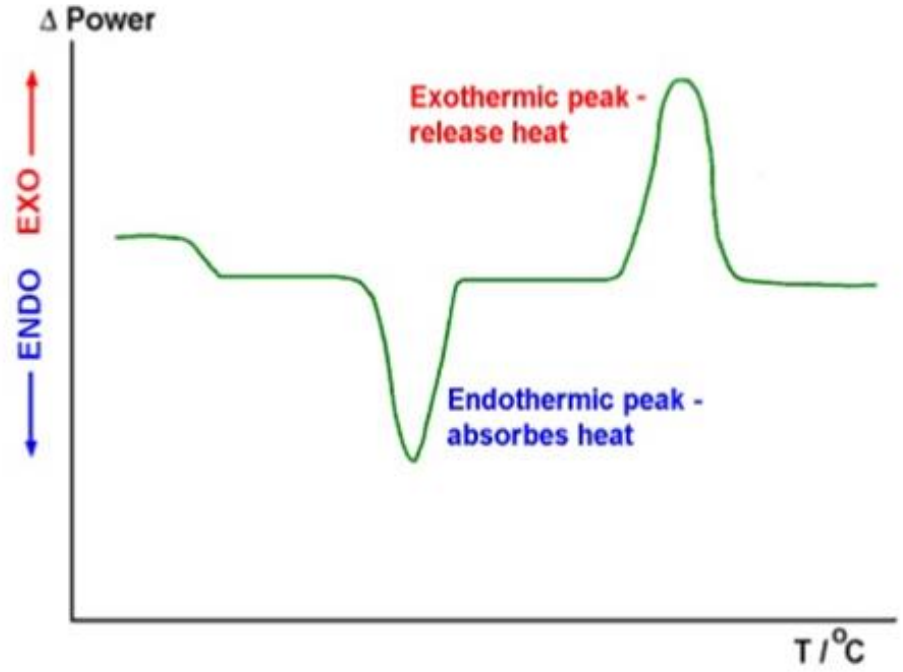

Figure 11. Graphical representation of DSC analysis.

2.1.4. Thermogravimetric analysis (TGA)

TGA [72] (Figure 12) is a technique for evaluating the mass change over time, or temperature, in a sample subjected to a heating treatment. These analyses can be conducted in both inert and reactive atmospheres, thus having information on the stability and reactivity of materials under different conditions.

The instrument used to perform these measurements consists of:

- Thermogravimetric balance with sensitivity of the order of μg and very accurate;
- Sample holder crucible;
- Furnace, which works at temperature generally between 25° C and 1500°C;
- Purging system, crucial for the diffusion of heat in every point, ensures an inert or reactive environment depending on how the measurement has to be performed;
- Data processing and visualization software.

Figure 12. TGA Instrument.

The experiment data are shown in the thermogram in which temperatures or time are marked along the abscissas, while in the ordinate the mass variation or its percentage value is reported. In addition to the components listed above, the steam generator was also used, which allowed to properly study the materials in hydration reactions, varying the atmosphere inside the chamber from inert (N_2) to water vapour.

As mentioned, when a sample is subjected to a temperature treatment, it can undergo different thermal events, the main ones being summarized in Table 8:

Table 8. Main thermal events during a thermogravimetric analysis.

A (s1) → A (s2)	Phase transition
A (s) → A (l)	Fusion
A (s) → A (g)	Sublimation
A (s) → B (s) + C (g)	Decomposition
A (glass) → A (rubber)	Glass transition
A (s) + B (g) → C (s)	Oxidation
A (s) + B (g) → C (g)	Combustion/volatilization

2.2 Synthesis

2.2.1 Sample Preparation

Evaluated the lack of commercial sufficiently-pure tricalcium aluminate, several efforts went into developing an efficient synthetic strategy to obtain the desired material. Tricalcium aluminate preparation was approached by both solid–solid synthesis and co-precipitation. For solid–solid synthesis, a mixture of calcium oxide (CaO) and aluminum oxide (Al_2O_3) at molar ratio $CaO:Al_2O_3$ = 3:1 and previously sieved (35μm), was put in a flask with 10 mL of ethanol and then sonicated for 30 min to obtain a homogeneous dispersion. Subsequently, the mixture was calcined in air at 1100 °C for 2 h. Of course, the obtained material after calcination was totally dehydrated, so to hydrate the material, the powder was put in a crucible, closed in a Teflon bottle containing a small amount of water at the bottom, and then kept at 180°C for 1h.

The co-precipitation was performed by adding aqueous sodium hydroxide (NaOH) through a peristaltic pump (2mL/min) to a solution containing Ca^{2+} (from $Ca(NO_3)_2 \cdot 4H_2O$) and Al^{3+} (from $Al(NO_3)_3 \cdot 9H_2O$). In this case, two different Ca/Al molar ratios were investigated, 1:1 and 3:2. The white precipitate aged overnight, was then vacuum-filtered (0.22μ), washed and finally dried at 105°C for 12 h to remove the residual water. Starting from the experimental evidence obtained by the two different approaches, an additional preparation method was developed as a combination of the two previous exposed. With this, co-precipitated material was treated at the same way as solid-solid sample, then calcination in air at 1100°C, followed by hydration by means of an hermetically close system. This procedure was defined as PCH (precipitation - calcination - hydration) method. Figure 13 offers a schematic vision of the PCH method.

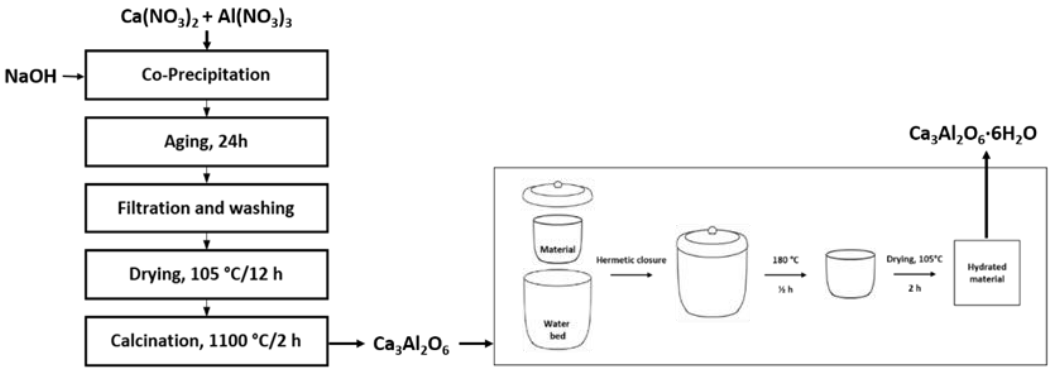

Figure 13. PCH method flowchart.

A deep discussion of the structural and chemical properties of the products obtained from the three syntheses, will be dealt later in the results chapter.

2.2.2 Sample Hydration

Further consideration about the sample hydration are discussed in this paragraph. Hydration step required particular attention due to the complexity of the processes occurring when calcium aluminates are put in contact with water: several reactions may occur and the temperature dependence cannot be disregarded. In fact, the most stable hydrate form is $Ca_3Al_2O_6{\cdot}6H_2O$, but its nucleation is extremely slow at low temperatures, and it is always preceded by the formation of metastable hydrates, which could persist for a long time before a thermodynamic conversion process occurs. Previous studies demonstrated that, during the primary stage of hydration, at temperatures between 15 and 70 °C, $CaAl_2O_4{\cdot}10H_2O$ and $Ca_2Al_2O_5{\cdot}8H_2O$ are mainly formed, while $Ca_3Al_2O_6{\cdot}6H_2O$ becomes consistent only at temperatures above 70 °C [73]. A correlation between the hydration temperature and the main formed calcium aluminate phase is summarized in Table 9.

Table 9. Calcium aluminates most frequently obtained, based on the hydration temperature [74]**.**

Hydration Temperature (°C)	Main Formed Phase(s)
<15	$CaAl_2O_4{\cdot}10H_2O$
15-27	$CaAl_2O_4{\cdot}10H_2O$/$Ca_2Al_2O_5{\cdot}8H_2O$
27-70	$Ca_2Al_2O_5{\cdot}8H_2O$/$Ca_3Al_2O_6{\cdot}6H_2O$

>70	$Ca_3Al_2O_6 \cdot 6H_2O$

Following these considerations, the samples obtained by the synthesis procedure were hydrated via the procedure described below: inside a teflon botte of ~100mL capacity, the sample (≈100 mg) and a bed of water were placed, respectively. The system was hermetically closed and heated for 30 min at 180 °C. Under these conditions, the generated high-pressure vapor favored the material hydration. Drying, later, at 105 °C to eliminate the non-chemically bonded water. The samples were weighed before and after this treatment, thus verifying the occurred mass change. In order to validate the procedure repeatability, for each batch, three replicas were done.

2.3 Characterization

2.3.1 Structural and Morphological Characterization

In order to clarify the chemical transformation of the materials during preparation and also after cycling tests, they were characterized structurally and morphologically by diffraction (XRD) and scanning microscopy (SEM). XRD measurements were conducted employing a Bruker D8 Advance instrument equipped with a Cu K monochromatic radiation source (40 kV, 40 mA). Bragg-Brentano theta-2theta configuration and a scan rate of 0.1 °/s were used to examine samples within the range 2θ 10-80°. Phase identification was performed using the PDF-4+ - ICDD database. SEM micrographs were collected by a Quanta 450 FEI with a Large-Field Detector (LFD), on Cr-coated samples with an accelerating voltage of 5 kV in high vacuum (10^{-6} mbar). Energy dispersive X-ray analysis (EDX) was also employed to collect point elemental analyses.

2.3.2 Thermal characterization

DSC analysis (Q100, TA Instruments) was performed to determine the quantity of involved dehydration heat. Specifically, 6–7 mg hydrated sample was put in an aluminum pan, covered with an aluminum cap and pressed during a sample crimper. On the cap, a micro hole was made to make sure that the formed vapour exited during the analysis. This precaution avoids a pressure increase inside the pan because of vapor formation. Measurements were performed in argon flow (N_2, 50 mL/min). Preliminarily, all samples were maintained at 105 °C for five min to get rid of the moisture content, and subsequently, a continuing heating step (10°C/min) up to 400 °C was applied.

Thermogravimetric analysis (TGA), performed by a STA 449 F3 Jupiter (Netzsch, Selb, Germany), was used to study the dehydration/hydration cycles and stability. The Thermo-gravimetric (TG) unit is coupled to an evaporation system for the vapour supply. After a preliminary sample (≈20 mg) drying at 125 °C in inert

gas flow (N_2 flow rate: 100 mL/min) for 60 min, each dehydration/hydration cycle was performed by the subsequent procedure:

1. Heating. The temperature was increased (10 °C/min) up to the chosen dehydration temperature (T_d = 250 °C);
2. Isothermal. The sample was held at these conditions for 120 min, for the whole dehydration reaction;
3. Cooling. The temperature was decreased (-10 °C/min) to the hydration temperature (T_h = 125 °C);
4. Stabilization step. Performed after cooling the temperature right down to the preset value, and so, this interval is important to stabilize the system temperature before the subsequent step.
5. Hydration reaction. A gas mixture flow of water vapour (2.22 g/h) and N_2 (35 mL/min) was supplied (pH_2O/p = 0.58), and therefore the isothermal hydration reaction proceeded for 120 min;
6. Release of adsorbed water. Finally, the water vapour supply was stopped, and the sample was kept at 125 °C for 30 min under a continuing N_2 flow (100 mL/min) to get rid of the physically adsorbed water from the sample. Table 10 summarizes one TG cycle.

Table 10. Schematization of a single thermogravimetric cycle.

Step n°	Temperature (°C)	Atmosphere	Description	Time (min)
1	125→250	N_2	Heating	-
2	250	N_2	Isothermal	120
3	250→125	N_2	Cooling	-
4	125	N_2	Stabilization	-
5	125	N_2	Hydration	120
6	125	N_2	Release of adsorbed water	30

3. RESULTS AND DISCUSSION

3.1. $Ca_3Al_2O_6$ Synthesis in Anhydrous and Hydrated Forms

As discussed previously, two preparation methods were initially attempted to get $Ca_3Al_2O_6$.

3.1.1. Solid-solid

Figure 13 below shows the diffraction patterns of the material after calcination (a) and subsequent hydration (b). The product did not show tricalcium aluminate peaks after calcination, while it was possible to mainly identify the presence of unreacted CaO (JCPDS # 70-4068) and aluminum oxide, Al_2O_3 (JCPDS # 34-0440). Furthermore, peaks related to mayenite, $Ca_{12}Al_{14}O_{33}$ (JCPDS # 09-0413) could be identified. Hence, under the applied conditions, the solid–solid synthesis did not lead to the formation of tricalcium aluminate. Probably, temperatures close to melting point (above 1350 °C) or multiple sequences grinding-calcination are necessary to obtain this product, through this method. What is worth to observe is a mayenite-to-katoite conversion after hydration, where $Ca_3Al_2O_6{\cdot}6H_2O$ (JCPDS # 24-0217) is present and no more anhydrous $Ca_{12}Al_{14}O_{33}$ peaks are observable. Gibbsite, $Al(OH)_3$ (JCPDS # 33-0018) and calcium hydroxide, $Ca(OH)_2$, were also present as hydrated products. Moreover, the characteristic peaks of unreacted Al_2O_3 were still evident, and calcium oxide was partially converted into calcite, $CaCO_3$ (JCPDS # 83-1762). The material had a low crystallinity after hydration as the background line clearly shows.

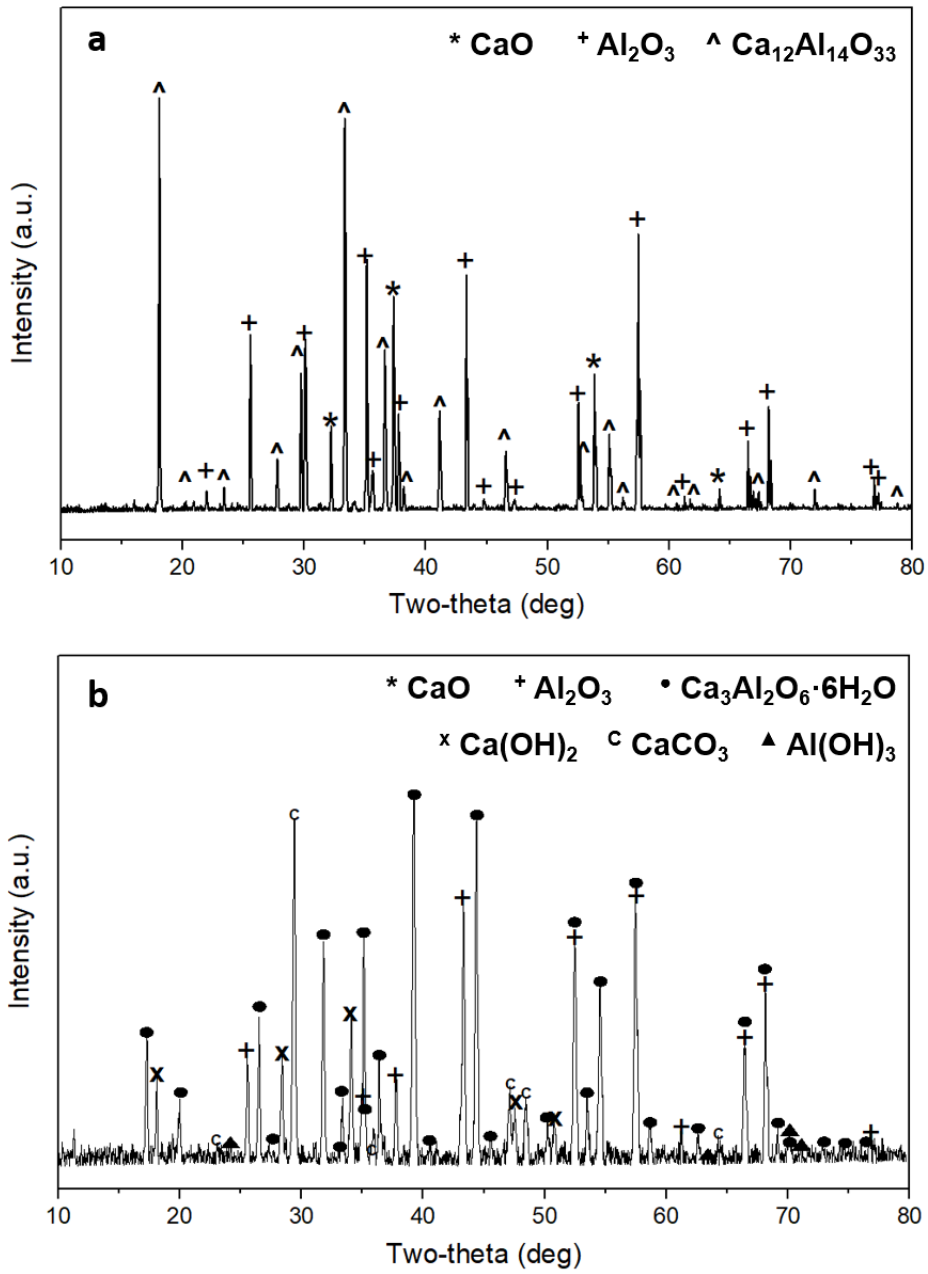

Figure 13. Diffraction patterns after calcination (a) and after hydration (b) for the solid-solid synthesis product. (JCPDS reference cards: CaO: 70-4068; $Ca_{12}Al_{14}O_{33}$: 09-0413; Al_2O_3: 34-0440; $Ca_3Al_2O_6{\cdot}6H_2O$: 24-0217; $Al(OH)_3$: 33-0018; $Ca(OH)_2$: 44-1481; $CaCO_3$: 83-1762).

SEM image of the product after calcination (Figure 14a) shows sintered particles, some of them relatively big (>5μm, black circle). After hydration (Figure 14b), the presence of big particles can still be noted (black circle), however it is also possible to observe other morphologies, the most evident one is the typical cubic shape of α-alumina (green arrow). EDX punctual analysis on a cubic particle confirmed a

local large excess of aluminum, with a Ca/Al molar ratio < 0.1. Plate particles, typical morphology of katoite, were also present (black arrow) and the punctual elemental analysis on these particles resulted on a Ca/Al ratio close to 1.5, corresponding to the $Ca_3Al_2O_6 \cdot 6H_2O$ one.

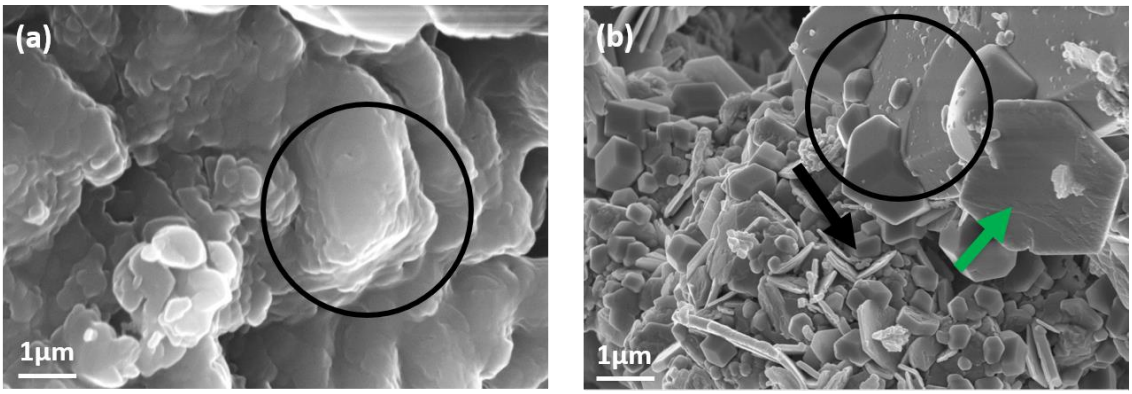

Figure 14: Scanning electron microscopy (SEM) images at magnification = 100 k after calcination (a), and hydration (b) for the solid-solid synthesis product.

3.1.2. Co-precipitation

XRD phase identification of the co-precipitated material is showed in Figure 15. Although an accurate washing, nitrate ions could not be completely separated from the product, as the main phase is $Ca_4Al_2O_6(NO_3)_2 \cdot 10H_2O$ (JCPDS # 54-0849). A small amount of tricalcium aluminate, with undefined number of water molecules $Ca_3Al_2O_6 \cdot xH_2O$ (JCPDS # 02-0083) is also identifiable. From the XRD patterns of the solid-solid and co-precipitation products it is obvious that the two methods were not useful to obtain a sufficiently pure product containing tricalcium aluminate hexahydrate.

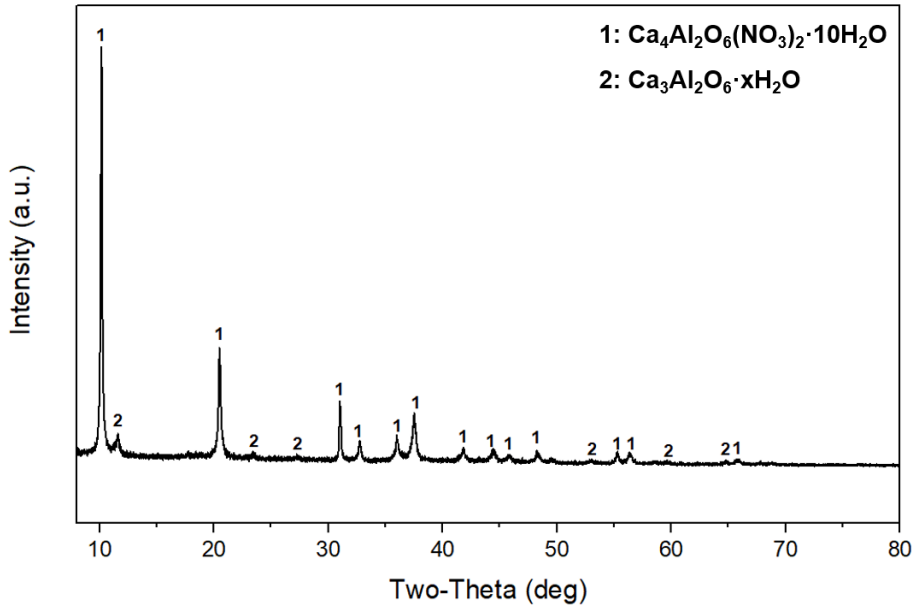

Figure 15. Diffraction pattern for the co-precipitation synthesis product. (JCPDS reference cards: $Ca_4Al_2O_6(NO_3)_2 \cdot 10H_2O$: 54-0849; $Ca_3Al_2O_6 \cdot xH_2O$: 02-0083).

For both materials, named CA-S and CA-P respectively for solid-solid and co-precipitation methods, the thermochemical behavior will be described below. SEM image (Figure 16), shows an almost unique irregular plate morphology, associable with $Ca_4Al_2O_6(NO_3)_2 \cdot 10H_2O$ (punctual analysis: Ca/Al ~ 2). Smaller particles could be probably $Ca_3Al_2O_6 \cdot xH_2O$.

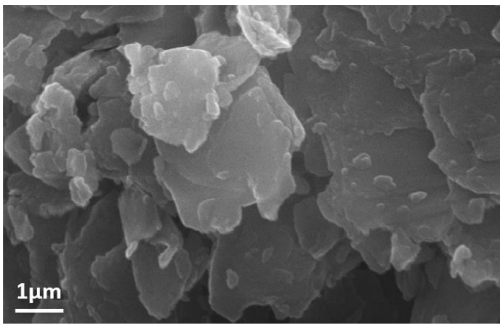

Figure 16: Scanning electron microscopy (SEM) images at magnification = 100 k for the co-precipitation product.

3.1.3. PCH method

Developing the PCH method meant starting from the experimental evidence obtained by the two previous approaches, in which it was observed that the calcination-hydration had led to an excellent conversion of mayenite to katoite, despite the fact that not negligible quantities of unreacted starting products were still present. At the same time, co-precipitation showed how a better interaction between Calcium and Aluminum ions can be achieved when passing through an aqueous solution. The purpose of this process was therefore to ensure the formation of a product by precipitation where the ions were incorporated within the same structure and also to favor the structural rearrangement and decomposition of the nitrate ions through calcination and, finally, to convert the product in its hydrated form.

The study of this method was carried out by performing two syntheses where the Ca/Al molar ratio was 3:2 and 1:1. As it can be observed in Figure 17a, both products 3:2 and 1:1 consisted of $Ca_3Al_2O_6$ (JCPDS # 38-1429). For 3:2, a small

presence of calcium oxide, CaO, was confirmed (JCPDS # 70-4068). On the other hand, a moderate amount of mayenite was also appreciable on 1:1.

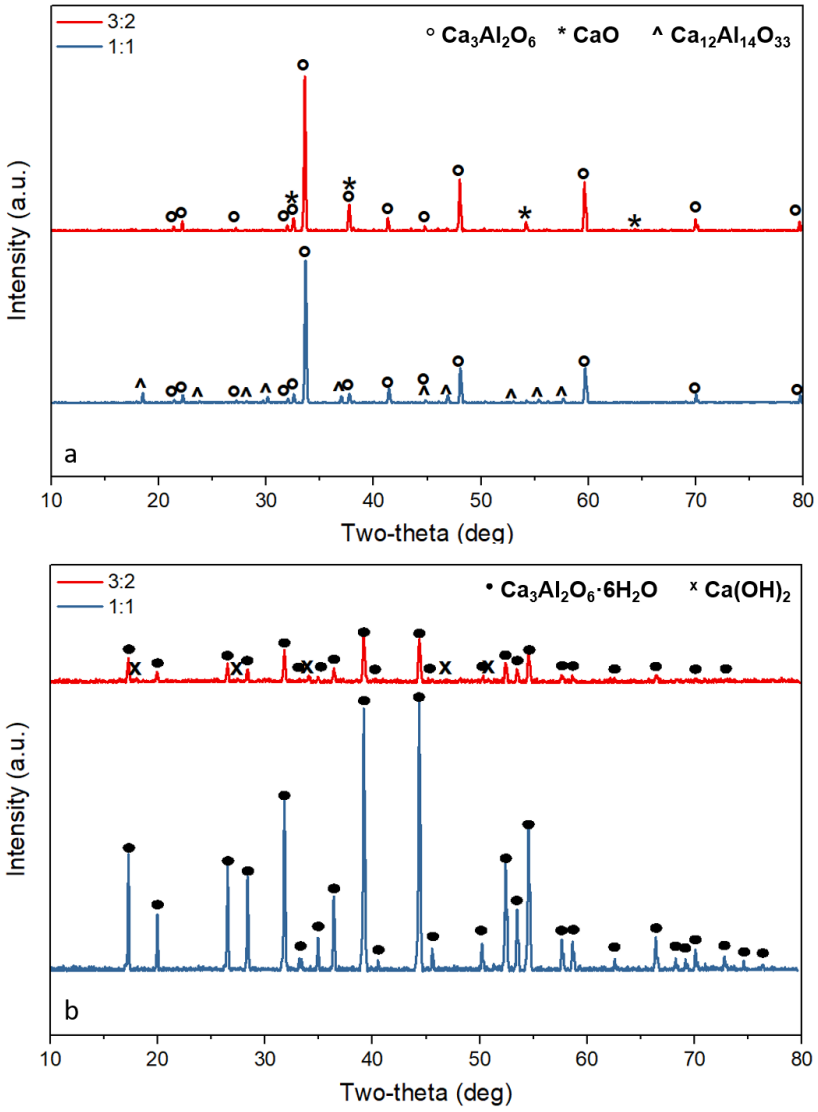

Figure 17. Diffraction patterns after calcination (a) and after hydration (b) for PCH products. (JCPDS reference cards: $Ca_3Al_2O_6$: 38-1429; CaO: 70-4068; $Ca_{12}Al_{14}O_{33}$: 09-0413; $Ca_3Al_2O_6·6H_2O$: 24-0217; $Ca(OH)_2$: 44-1481).

For TES application, a relevant aspect that requires attention to assess the potential suitability of the material in this context is to evaluate the hydrated phases that are formed due a hydration process. In particular, Figure 17b shows the diffraction patterns after the hydration step. For 3:2 Ca/Al molar ratio sample, katoite, $Ca_3Al_2O_6·6H_2O$ was detected. A small amount of calcium hydroxide, $Ca(OH)_2$, was also observed, formed by the hydration of calcium oxide observed in Figure

17a. The diffractogram showed low intensity peaks. In 1:1 Ca/Al molar ratio sample, only the characteristic peaks of katoite, $Ca_3Al_2O_6 \cdot 6H_2O$, were present, thus indicating that, besides the hydration of the $Ca_3Al_2O_6$ phase, mayenite was also converted into the most thermodynamically stable katoite. The obtained results demonstrated that $Ca_3Al_2O_6$ was almost quantitatively achieved by the PCH method using a Ca^{2+}/Al^{3+} molar ratio 1:1, which was in defect of the calcium amount with respect the stoichiometry of $Ca_3Al_2O_6$, and it was fully converted into the hexahydrate form. With regard to the co-precipitation products, it is important to point out the discrepancy between what could be expected from the initial Ca/Al ratio and what is shown by the diffraction patterns of materials 3:2 and 1:1, in terms of phase composition. A rational explanation is given by the acid–base behavior of aluminum cations: amphoteric behavior of Al^{3+} makes its solubility increasingly relevant after pH ~9, in accordance with the tetrahydroxy-aluminate ion formation, as described in Equation (15).

$$Al(OH)_{3(s)} + OH^-_{(aq)} \rightleftarrows Al(OH)_4^-{}_{(aq)} \quad (15)$$

It is therefore understandable that part of the initially employed aluminum was not found in the final product. Consequently, having an initial molar ratio of 3:2, some of Ca^{2+} precipitated as $Ca(OH)_2$ (dehydrated to CaO, subsequently, during calcination), while using an initial ratio 1:1, the aluminum excess led to the formation of tricalcium aluminate.

The morphology of the samples after calcination is shown in Figures 18a, b. A similar morphology is observable for both samples, in which rounded particles (red arrows) and flat hexagonal particles of different sizes (black arrows), ascribable to tricalcium aluminate, are present.

Furthermore, after hydration (Figures 18c, d) hexagonal katoite plates can be noted (black arrows); these have a more regular shape in 1:1 batch, in which katoite XRD peaks are also more intense. The punctual elemental analysis on these particles confirmed a Ca/Al ratio close to 1.5. The 3:2 sample clearly shows a significant amount of calcium hydroxide nanoparticles (blue arrow), where the elemental analysis gave a significantly increased Ca/Al molar ratio (>10).

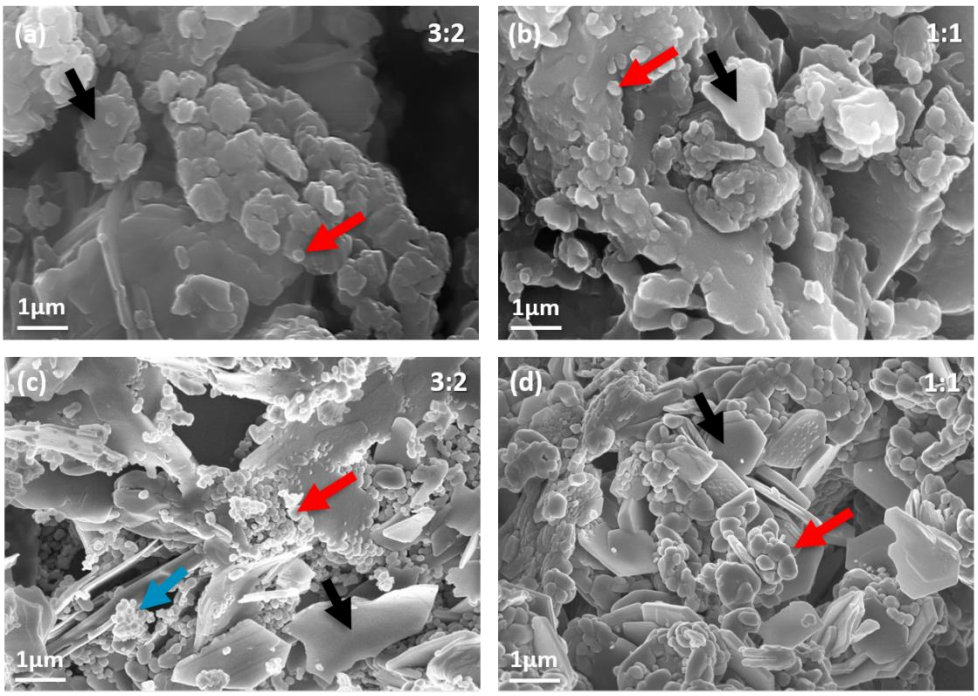

Figure 17. SEM images at magnification = 100 k after calcination (a, b) and hydration (c, d) of PCH products.

For simplicity, the materials obtained via the three procedures will be named with different codes in the next paragraphs. Table 11 resumes the samples code for the materials and the preparation method.

Table 11. Samples code and preparation method.

Sample Code	Method
CA-S	Solid-solid
CA-P	Co-precipitation
CA-11	PCH
CA-32	PCH

3.1.4. Structural evolution during calcination: a detailed investigation

Since the thermal treatment of co-precipitated materials involves a deep structural and chemical rearrangement, this aspect has been investigated by comparing various calcination temperatures. Portions of material from the same batch (CA-11), were calcined for 2h in air at temperatures of 500 °C, 700 °C, 900 °C, and

1100 °C. Figure 18 shows the representative diffraction spectra of the batch as a function of the calcination temperature. By evaluating the XRD spectra evolution at increasing calcination time, a clear relationship between thermal treatment and sample crystallinity can be observed. A calcination temperature of 500 °C leads to a poor crystallinity. The aluminum is mainly present in the form of calcium dialuminate, $CaAl_2O_4$ (JCPDS # 01-0888), and calcite, $CaCO_3$ (JCPDS # 83-1762), while calcium aluminate nitrate hydroxide is not appreciable.

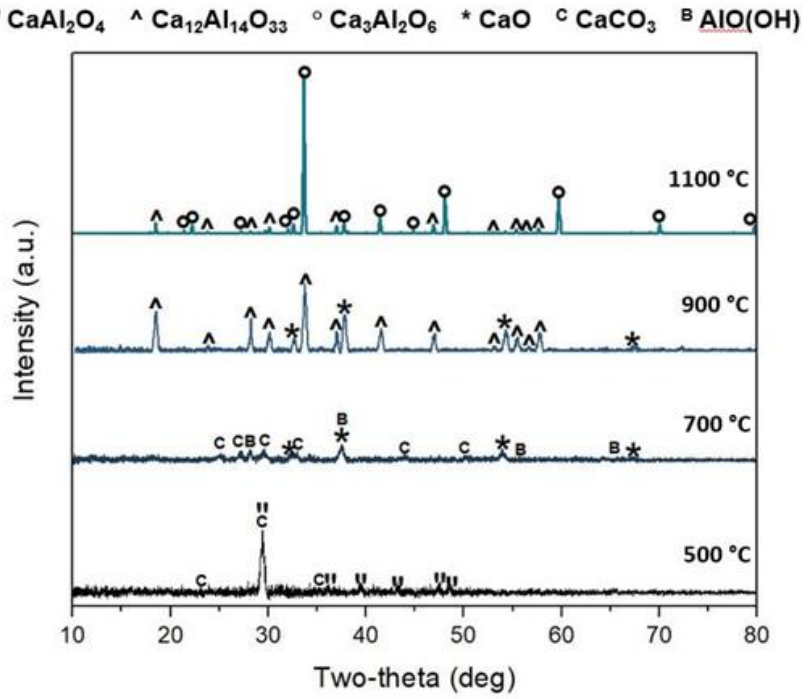

Figure 18. CA-11 PCH material diffraction patterns after 2 h calcination under static air at 500 °C, 700 °C, 900 °C and 1100 °C ($CaAl_2O_4$: 01-0888; $Ca_{12}Al_{14}O_{33}$: 09-0413; $Ca_3Al_2O_6$: 38-1429; CaO: 70-4068; $CaCO_3$: 83-1762/19-3758; AlO(OH): 78-4581).

After calcination at 700 °C, the sample still presents amorphous phases; however, some peaks related to crystalline phases are identifiable. Calcium carbonate partially decomposes into calcium oxide (JCPDS # 70-4068), while the remaining portion is converted into vaterite, $CaCO_3$ (JCPDS # 19-3758). Aluminum is observable only as boehmite, AlO(OH) (JCPDS # 78-4581). The diffraction pattern continues its evolution after calcination at 900 °C, where the crystallinity increases and the main phase is mayenite, $Ca_{12}Al_{14}O_{33}$ (JCPDS #09-0413).

Additionally, peaks of calcium oxide are also observable, demonstrating a complete decarbonation of the previously detected calcium carbonate phases. As the latest diffraction pattern show, tricalcium aluminate, $Ca_3Al_2O_6$ (JCPDS # 38-1429), appear predominantly only after calcination at 1100 °C; however, a low amount of mayenite is still present.

3.2 Dehydration and heat of reaction

In order to thermally characterize the materials, thermogravimetric analysis and differential scanning calorimetry measurements were performed. TGA scan of the first dehydration process enabled the evaluation of the operating temperature range and the quantification of the related weight loss. DSC scan measured the amount of involved endothermic heat of the observed processes. The comparison of the thermogravimetric dehydration results of the various samples, shown in Figure 19, demonstrated that the dehydrated fraction at 350 °C was significantly influenced by synthesis process. Indeed, CA-11 sample showed the highest weight loss (21.12%), quite near the theoretical mass loss because of the katoite partial dehydration (Equation 16):

$$Ca_3Al_2O_6 \cdot 6H_2O_{(s)} \rightarrow Ca_3Al_2O_6 \cdot 1.5H_2O_{(s)} + 4.5H_2O_{(g)} \qquad (16)$$

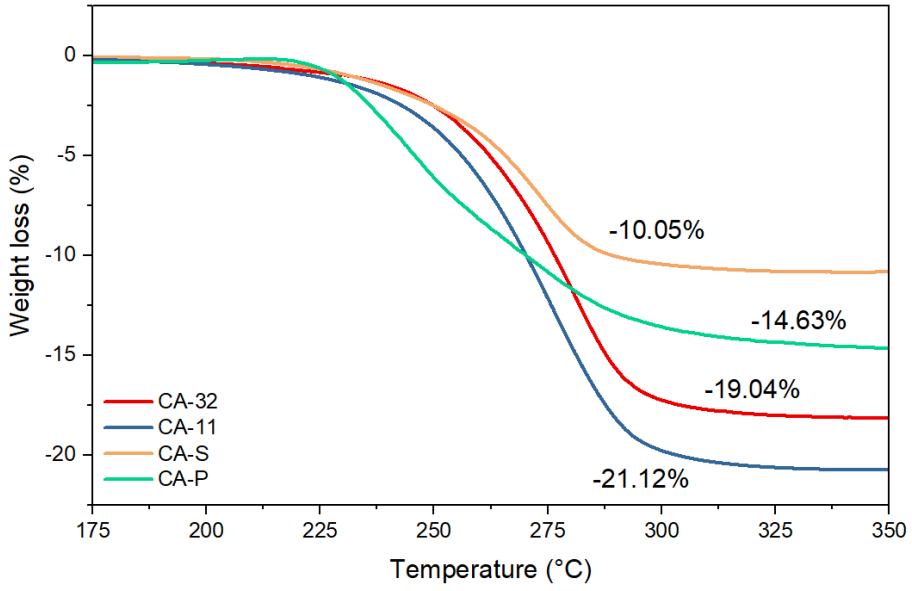

Figure 19. CA-32 (red), CA-11 (blue), CA-S (orange) and CA-P (green) thermogravimetric (TG) curves, recorded between 175 °C and 350 °C, scan rate 10 °C/min.

The mass loss decreased about 19.04% for CA-32 batch, 14.63% for CA-P and 10.05% for CA-S. Consequently, thermogravimetric curves showed a clearly more practical behavior for the PCH products compared to the others.

Furthermore, the dehydration enthalpy was determined through integration of the peak obtained by calorimetric analysis (Figure 20). The results confirmed what was highlighted by TGA measurements about the PCH products. CA-11 revealed a dehydration heat of 807.0 kJ/kg, beyond CA-32, which was quite high (655.8 kJ/kg), while CA-S and CA-P, respectively 530.2 kJ/kg and 244.3 kJ/kg. Observing those analyses, a preliminary explanation of the dehydration process is assessed: based on the XRD phase identification, the process is especially associated with the thermal decomposition of katoite for CA-11, -32, -S, which implies a 4.5 water molecules loss.

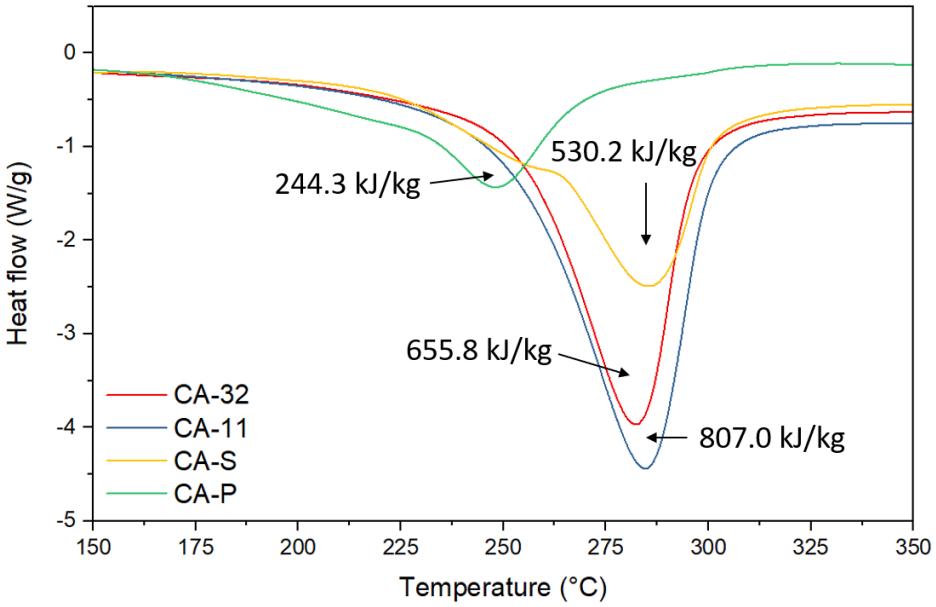

Figure 20. CA-32 (red), CA-11 (blue), CA-S (orange) and CA-P (green) calorimetric (DSC) curves, recorded between 150 °C and 350 °C, scan rate 10 °C/min.

This process occurs without any side-reaction for PCH products (calcium hydroxide phase does not interfere because of the higher dehydration temperature >350°C). In contrast, it's still possible to perceive that for CA-S product there is the presence of a further process, as a secondary DSC peak shows clearly, ascribed to the decomposition of aluminum hydroxide to boehmite (Equation 17):

$$Al(OH)_{3(s)} \rightarrow AlO(OH)_{(s)} + H_2O_{(g)} \qquad (17)$$

This result confirms that this batch is characterized by a relevant microstructural heterogeneity that hinders the hydration/dehydration efficiency. Co-precipitated CA-P material dehydrates early with respect to the others. Evidently, two or more processes occur simultaneously, as the complexity of the curves demonstrates. However, going into deep considerations of the involved reactions is beyond the scope of this discussion, especially after evaluating this material as the least performing. In contrast, the CA-11 and CA-32 samples show a microstructural homogeneity which acts effectively on the vapor phase mass exchange processes. The phenomenon, allows to reach high thermal capacities in a very narrow temperature range, enhancing the selectivity of the material for a suitable and efficient use of thermal waste. Table 12 summarizes the results obtained from the analysis.

Table 12. TGA and DSC characterization results.

Sample ID	T_{onset} (°C)	Weight Loss (%)	Heat (kJ/kg)	Katoite (%)
CA-32	247.5	-19.04	655.8	88.9
CA-11	245.8	-21.12	807.0	98.6
CA-S	248.7	-10.15	530.2	< 46.9
CA-P	174.8	-14.63	244.3	0

The last column shows the quantity of katoite, present in the studied material, it was determined through the conversion percentage compared to the theoretical reference value for pure katoite (−21.42 wt.%), calculated as follows (Equation 18):

$$\Delta m_{th} = - \frac{4.5 \cdot MW_{H2O}}{MW_{Ca3Al2O6 \cdot 6H2O}} \cdot 100 \qquad (18)$$

Regarding the CA-S material, the amount of katoite cannot be determined quantitatively, due to the existence of two simultaneous processes. Thus, in lack of further experimental evidence, it is only possible to claim that the sample has a katoite content lower than 46.9% (calculated assuming that the whole weight loss

is ascribed to the dehydration of the katoite phase). Different consideration are made for CA-P, for which zero content of katoite is attributed arbitrarily, because no katoite peaks were identified by XRD analysis. It is worth to clarify that this material was helpful to fully explain the difference between different approaches, but will not be considered next, due to its poor applicability in terms of complexity of the process and low dehydration heat.

3.3 Dehydration/Hydration Stability

3.3.1 Five cycles experiment

After structural and thermal characterization of synthesized materials, cyclic TG experiments were useful to assess the dehydration/hydration stability of the batches. Figure 21 shows the entire first thermogravimetric cycle for CA-11,-32 and –S. The highlighted sections 1–6 correspond to the analysis steps previously reported in the experimental section. The plot offers an immediate impact regarding the material's mass changes along each step, relating these transitions to the dehydration and hydration reactions.

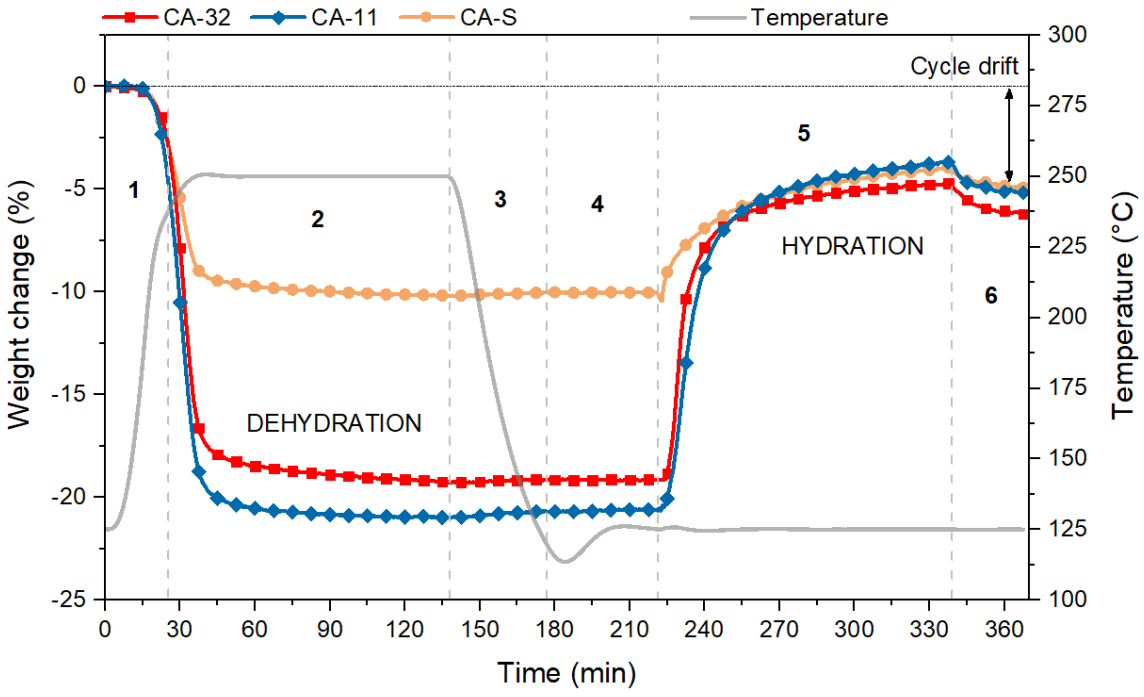

Figure 21. First dehydration/hydration cycle for CA-32 (red), CA-11 (blue) and CA-S (orange).

Initially, a heating phase and a subsequent isotherm at 250 °C were applied (steps 1 and 2). As shown, this temperature allowed the reaction to occur in a relatively short time. In fact, already at about 200–220 °C the dehydration began, but it was completed when the temperature plateau was reached. The time that lapsed between the achievement of the onset temperature and the end of the process (identified as weight loss stabilization) was around 40 min. The dehydration results at equilibrium were compatible to the previous TGA ones. This means that the chosen operating temperature was adequate to obtain a complete reaction conversion of the materials into their respective dehydrated forms. Step 3 and 4 were necessary after the dehydration reaction to decrease and stabilize the system temperature at 125 °C (hydration temperature) before the atmosphere shifted from inert to water vapour. Hydration kinetics on PCH batches was faster; the mass suddenly increased when the water vapor was supplied (5), reaching a plateau after 35–40 min. Overall, CA-32 exhibited a slightly higher hydration rate and, at the same time, a more marked slope variation. In contrast, CA-11 exhibited a larger yield at the end of the hydration process. However, both materials had a comparable hydration trend. This behavior could be of course related to their similar composition (katoite, mostly) and morphology (different sized hexagonal plates). CA-S had a different hydration kinetic; the mass gain associated to the hydration reaction was more gradual, if compared to the other two batches. This behavior could be related to its structural heterogeneity that kinetically limited the hydration processes. The release of physisorbed water (6) occurred when the water vapor supply was over and led to a small weight loss for all the materials; hence, it was deducted that just a limited portion of adsorbed water was not chemically bonded. However, to estimate the effective yield of the hydration reaction, this surplus of mass was not calculated, since the surface interaction with physisorbed water clearly had a weaker energy than a chemisorption. Hence, to avoid an overestimation of the released heat, the real hydration conversion in mass was calculated as the difference between the mass at the end of section 6 and the beginning of section 5. Additionally, in section 6, the cycle drift is evidenced (double pointed arrow). It shows a less hydration yield than the previous

dehydration, which led to an efficiency loss throughout the cycle. This aspect, therefore, involved an evaluation of the behavior in subsequent cycles. Table 13 lists the conversion values for each dehydration and hydration step, related to a five-cycle experiment. The reported data are expressed by means of $R_{d/h}$ (%), which is the normalized conversion obtained by Equation 19:

$$R_{d/h}(\%) = \frac{\Delta m_{d/h}}{\Delta m_{1^\circ d}} \cdot 100 \qquad (19)$$

where d and h refer to the dehydration and hydration steps, respectively. The term Δm refers to the mass variation at the end of the considered process, while $\Delta m_{1^\circ d}$ is the mass variation relative to the first dehydration, which is supposed to correspond to a 100% yield. Normalized conversions are a proper method to check how the materials work along the cycling, taking into consideration their different katoite content. The previously described cycle drift can be numerically evaluated by observing the hydration yields: PCH batches presented a comparable R_{h1° (66.5% and 67.49% for CA-32 and CA-11, respectively), while the solid–solid one was moderately lower (52.68%). The cycle drift, however, became less enhanced cycle by cycle. Figure 23 graphically shows how the materials behavior evolved during the experiment, plotting the normalized conversion for each cycle (dehydration on the left and hydration on the right) against time. CA-32 reached comparable conversions after the third cycle (R_h around 40%). Similar conversions were also appreciated for CA-11 for the last two cycles, around a R_h of 33%. CA-S sample, on the contrary, failed to reach a stable conversion throughout the experiment, and its conversion was still decreasing at the end of the fifth cycle (8.51%).

Table 13. Thermogravimetric performances per cycle.

Sample ID	Cycle	Dehydration T_{onset} (◦C)	Rd (%)	Rh (%)
CA-32	1	241.5	100	66.5
	2	231.1	67.6	50.9
	3	229.8	45.7	40.4
	4	230.2	40.4	40.2
	5	230.0	40.1	39.8
CA-11	1	242.7	100	67.5
	2	231.4	68.1	48.3
	3	229.4	47.6	37.1
	4	229.3	42.5	33.6
	5	229.6	33.3	32.5
CA-S	1	241.0	100	52.7
	2	233.2	51.0	31.7
	3	233.3	32.1	15.4
	4	231.7	12.2	11.0
	5	230.5	11.4	8.5

The progressive decrease suggests that the solid-solid material may become totally deactivated within the subsequent cycles. The non-purity of the CA-S sample had, therefore, a detrimental effect on the thermal stability of the hydration process. Still in Figure 23, it should be noted that the hydration kinetic of the second cycle undergoes a significant change with reference to the first cycle, then remains similar for the subsequent ones.

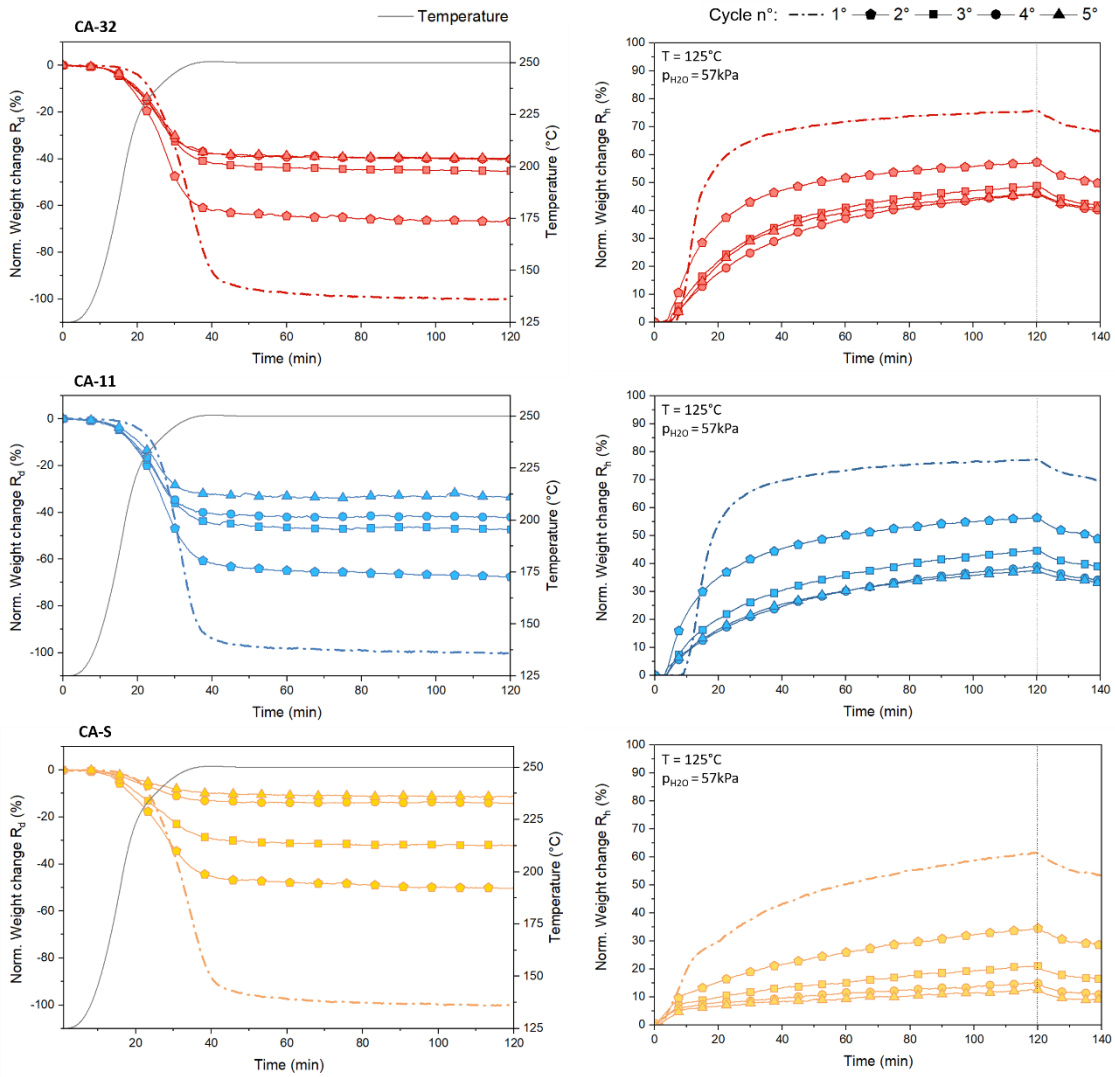

Figure 23. The 1st, 2nd, 3rd, 4th and 5th normalized dehydration/hydration curves for CA-32 (red), CA-11 (blue) and CA-S (orange).

An explanation may well be associated with a structural change that occurs during the first cycle, which involves rearrangements that persists until a condition of stability is achieved. The amount of cycles required to realize a structural stabilization really depends on the material features and conditions applied during cycling. As a consequence of the structural change that the materials gradually had, the dehydration onset temperature, T_{onset}, decreased linearly (see table 13). This temperature was found to be settled at an almost constant value from the third cycle for CA-11 and CA-32 (around 230 °C), simultaneously with an occurring conversion stabilization, as described before. For CA-S, contrarily, never stabilized and continued to decrease within the reaction yield. In order to Figure

out the heat efficiency of the materials, the amount of released heat per mass unit ($Q_{rel,m}$) and volume unit ($Q_{rel,V}$), referred by the single cycle (n), was calculated by Equations 20-21:

$$Q_{rel,m(n)} = Q_{DSC} \cdot \frac{R_{\%;h(n)}}{100} \quad (20)$$

$$Q_{rel,V\,(n)} = Q_{rel,m(n)} \cdot \rho \quad (21)$$

where Q_{DSC} is the previously dehydration heat, determined by calorimetric analysis, $R_{\%;h(n)}$ is the normalized hydration conversion referred by the n cycle and ρ is the experimentally determined bulk density for the hydrated materials, corresponding to 745 kg/m^3 for CA-32, 854 kg/m^3 for CA-11 and 699 kg/m^3 for CA-S. Figure 24 shows the released heat per mass unit (a) and volume unit (b) as a function of the cycle number (n).

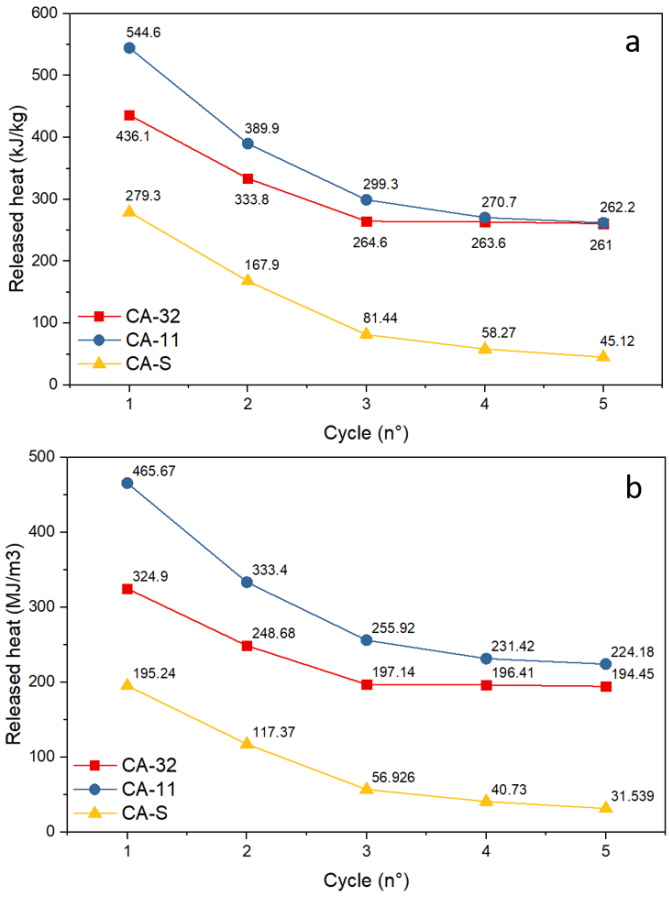

Figure 24. Released heat per mass unit (a) and volume unit (b) per cycle.

What will be observed in Figure 24a is that CA-11 has a notable performance drop during the five cycles, which brings to exchange a quantity of heat, numerically comparable to the CA-32 one. Furthermore, the trend of CA-11 material suggests that an extra small loss in efficiency can be potentially observed within the following cycles. CA-32 performances drop moderately and they are softened within the third cycle. In fact, the curve trend between the third and fifth cycles reached an almost constant value. Hence, a stabilization for the subsequent cycles is expected. CA-S showed a progressive decreasing of exchanged heat, reaching the value of 45.12 kJ/kg. Similar considerations regarding PCH batches will be argued from Figure 24b; however, there's an interesting difference due to the higher density of CA-11, which ensures a greater efficiency, despite the lower reaction yield. The materials were structurally and morphologically characterized again by XRD and SEM after cyclic experiment. In Figure 25, the diffraction patterns of the materials are shown.

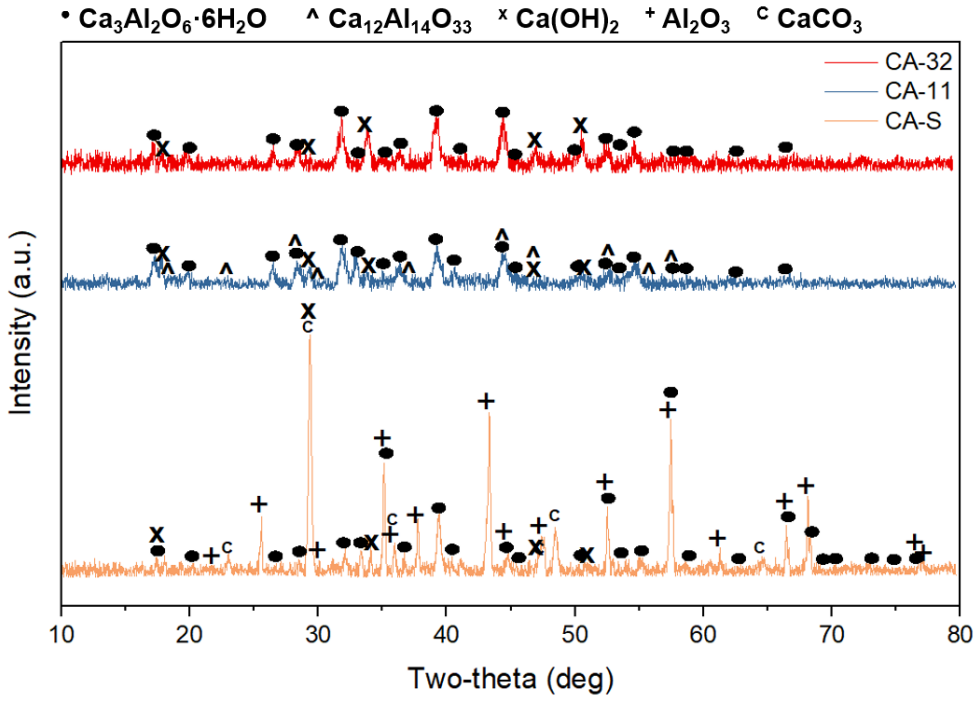

Figure 25. Diffraction pattern after the five-cycle experiment for CA-32 (red), CA-11 (blue) and CA-S (orange). (JCPDS reference cards: $Ca_3Al_2O_6 \cdot 6H_2O$: 24-0217; $Ca_{12}Al_{14}O_{33}$: 09-0413; $Ca(OH)_2$: 44-1481; Al_2O_3: 04-2852; $CaCO_3$: 12-0489).

CA-32, which exhibited the best conversion and therefore the highest tendency to stabilize, has a quite similar diffraction pattern after the experiment in terms of phase composition, where katoite, $Ca_3Al_2O_6 \cdot 6H_2O$, and calcium hydroxide, $Ca(OH)_2$, are recognizable. No additional phases are identified. In CA-11, originally composed almost exclusively by katoite (98.6%) and still identifiable after five cycles, shows the further presence of characteristic peaks of mayenite, $Ca_{12}Al_{14}O_{33}$, and calcium hydroxide. This will be justified, considering that katoite suffers a partial decomposition, which is reasonably associated to the formation of mayenite aggregates and the consequent release of calcium oxide CaO, subsequently converted in the hydroxide form by the vapor atmosphere. A possible reaction scheme may well be (Equations 22-23):

Under heating:

$$7Ca_3Al_2O_6 \cdot 6H_2O_{(s)} \rightarrow Ca_{12}Al_{14}O_{33(s)} + 9CaO_{(s)} + 42H_2O_{(g)} \quad (22)$$

Under water vapor supply:

$$CaO_{(s)} + H_2O_{(g)} \rightarrow Ca(OH)_{2(s)} \quad (23)$$

Moreover, broadening and fewer intensity of the peaks, compared to the starting materials, indicate a less crystallinity. CA-S, characterized by the lowest conversion value, still exhibits typical katoite peaks, although less intense. Similarly to CA-11, mayenite peaks are visible as a consequence of katoite decomposition. The main crystalline phase is alumina, Al_2O_3, which prevents the process reversibility. In fact, the high stability of the aluminum oxide inhibits its rehydration step. Calcium oxide, which was present in the initial material, is not identified anymore; it is likely that the contact with atmospheric carbon dioxide has led to a total conversion of the latter into calcium carbonate (Equation 24), $CaCO_3$, already detected on the pristine material.

$$CaO_{(s)} + CO_{2(g)} \rightarrow CaCO_{3(s)} \quad (24)$$

CA-S was composed at the beginning by aluminum hydroxide as well, this phase is no longer observable because of its decomposition during the cycles; in fact, as mentioned above, boehmite (AlO(OH)) was formed during the first dehydration process, and subsequently, it is possible to reason that this phase is slowly converted into alumina. This suggestion is also supported by the slow hydration kinetic, which aluminum oxides and oxides hydroxides present. SEM images shown in Figure 26 (magnification = 100 k) lead to further considerations regarding the investigated materials. Comparing samples morphologies before (Figures 14 and 17) and after (Figure 26) cycling, some differences are observable. In particular, CA-32 is characterized by rounded nanoparticles around 100–200 nm (calcium hydroxide), homogeneously distributed, covering hexagonal plates (katoite).

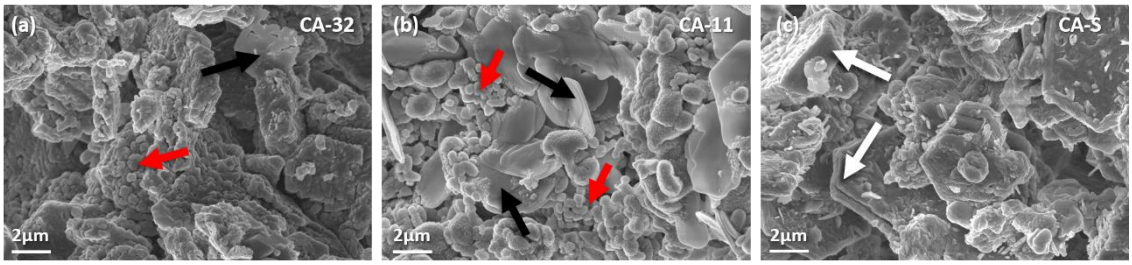

Figure 26. SEM images, magnification = 100 k, for CA-32 (a), CA-11 (b) and CA-S (c) after five dehydration-hydration cycles.

In contrast, CA-11 is characterized by nanoparticles, probably mayenite and calcium hydroxide (red arrows), deposited on coalesced hexagonal plates of katoite (black arrows). Again, the smaller particle size after five cycles could be related to the less crystallinity evidenced before. CA-S still shows less uniformity: large particles are predominantly observed (white arrows) and different structures, as confirmed by XRD analysis, are present. The detected morphological and structural materials modifications can address the various behavior of CA-11 and CA-32 materials. The absence of decomposition processes of katoite in CA-32 may be associated with the presence of hydrated oxide impurities. This phase could play a fundamental role in terms of surface basicity by promoting an improved thermodynamic stability of katoite, avoiding the formation of mayenite, instead described for CA-11 and CA-S, thus ensuring a bigger conversion.

Accordingly to this, it is reasonable to assume that the surface basicity imposed by $Ca(OH)_2$ explains the stabilization observed for CA-11 (in which calcium hydroxide is produced during the cycling), and also the yield difference may be due to the formation of mayenite during this second case, which involves a loss of the active portion of the material.

3.3.2 Further consideration on cycling for TES application

Certainly, the experiment shown in the previous paragraph is indicative of how the preparation technique, as well as the calcium-aluminum ratio used for the preparation of the material, affect the way it operates during charge/discharge cycles. It is easy to understand how, in a practical way, the conversion data obtained and shown in table 13 are not yet sufficient to justify the use of PCH materials for TES applications. However, it should be noted that the conversion percentage is strongly dependent on the type of apparatus which is used and it is therefore not very indicative to consider only the data obtained from a small system where the instrumental setup significantly affects performances. For instance, in the instrumentation used for the experiment, the hydration reaction, which certainly represents the limiting step in the operation of the material, can only be carried out within a narrow temperature range and at partial steam pressures not exceeding 0.9. In addition to this, the pressure inside the system cannot be different from the atmospheric one. It is therefore right to underline that the experiment does not provide real data about the conversion of the material, given the limited conditions, but at the same time it is very useful to understand how PCH materials can be applied due to their stabilization against subsequent reactions of dehydration/hydration.

In order to better understand how the material behavior is influenced by the boundary conditions, the CA-11 material was subjected to a different cyclic experiment, in which more appropriate hydration conditions could be implemented. To be more precise, the dehydration was performed under the same temperature conditions as the previous experiment, i.e. by TGA heating from 105 °C up to 250 °C (10 °C/min) and isotherm of 25 min (sufficient time as already

seen to ensure complete reaction), while hydration was performed on the material within the same hermetic Teflon system used to convert the materials from the totally anhydrous to the hydrated phase during the synthesis procedure. A pattern of the cycle, which was repeated five times, is shown in Figure 27.

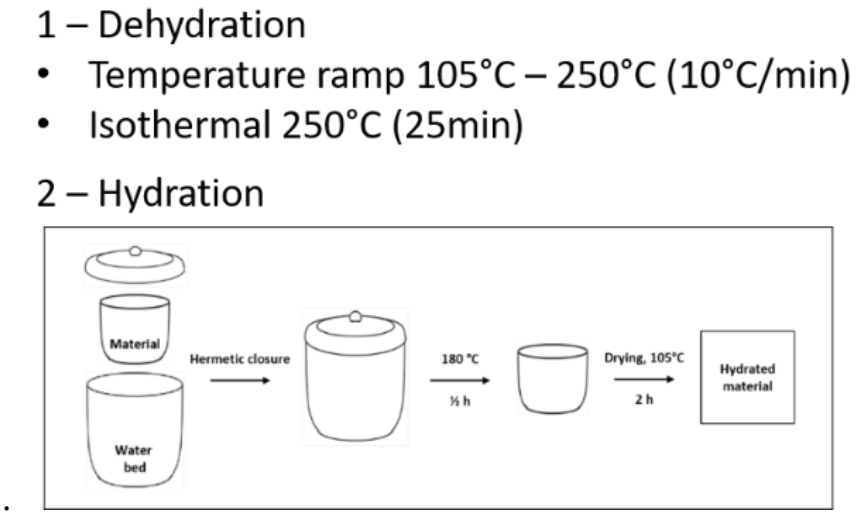

Figure 27. TGA-hermetic system cycle scheme.

It is obvious that by performing the hydration reaction within such a system it is not possible to monitor the mass variation and therefore all information regarding, for example, the kinetics of the process is completely disregarded. On the other hand, it was possible to determine the pressure conditions inside the reactor as follows: the internal volume of the system was measured and the volume of the crucible containing the material was subtracted from this. For each cycle, the same known amount of water was introduced into the system and, by applying the Van der Waals equation for real gases, the water vapor pressure was estimated to be around ~16 atm. Of course, the information on subsequent dehydration is of considerable importance because it derives directly from the amount of material that has been previously hydrated.

Therefore, observing Figure 28 below where the five dehydrations of the material are reported, some behavioral analogies along the cycles are still observable: clear decrease in yield between the 1st and 2nd cycle, variation of the dehydration curve (kinetics) and T_{onset} decrease (which also in this case settles on a value around 230 °C). Also in this case the material needs some "preliminary" cycles before reaching

a stabilization, but the yield is much higher than that obtained with the previous setup. Making a comparison in terms of stored heat per volume unit at the fifth cycle, ideally, the material would have a capacity of 603.4 MJ/m^3, compared to less than half (229.5 MJ/m^3) in the previous case.

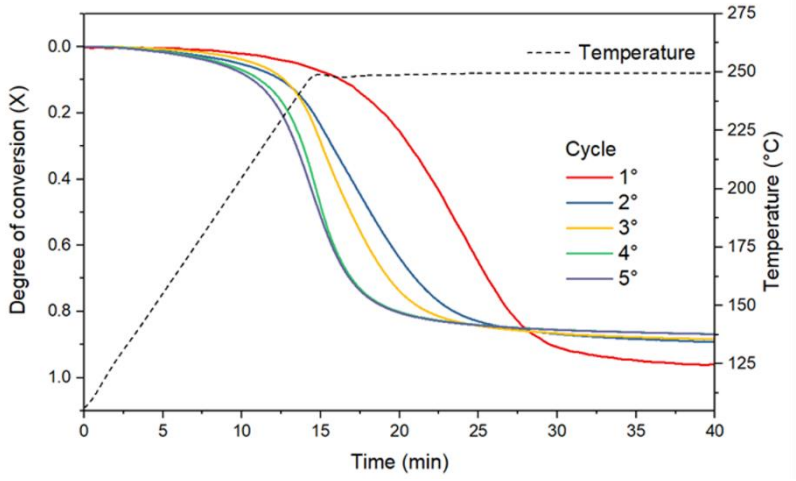

Cycle	R_d (%)
1	100
2	89.65
3	88.81
4	87.82
5	87.75

Figure 28. Five dehydration cycles for CA-11 after hydration on hermetic system.

Once again, it should therefore be clarified that this kind of consideration must be made exclusively depending on the working conditions. However, having established that a material can have a role in TES field, it is certainly the next step to find the right placement system, in order to increase its performances.

3.4 Latest development – in progress

In this last section, some partial results regarding the recent developments on the study of tricalcium aluminate hexahydrate are exposed.

3.4.1 Thermodynamic evaluation of the working pair

In the light of what was described before, the right way to assess a material and then compare it to other ones is a thermodynamic description based on parameters that are independent to the applied conditions. Additionally, the tricalcium aluminate hexahydrate/1.5-hydrate pair is still poorly studied, and a study on thermodynamics is needed in order to describe its features as a TCM. In particular, this study was carried out with the aim of determining the turning temperature (T*) and the enthalpy variation ($\Delta_r H$) of the dehydration/hydration reaction. The turning

temperature is the temperature at which the constant of equilibrium of the reaction becomes unitary. Being $Ca_3Al_2O_6{\cdot}6H_2O/Ca_3Al_2O_6{\cdot}1.5H_2O$ an heterogeneous system, where the amount of the solid-state components does not interfere with the equilibrium, the constant is directly related to the partial pressure of the gaseous component (i.e. water vapor) raised to its stoichiometric coefficient (see eq. 25):

$$K_{eq} = \left(\frac{p_{H_2O}}{p}\right)^{4.5} \quad (25)$$

At equilibrium conditions, the free energy variation (ΔG) is equal to zero and a correlation between turning temperature and the enthalpy and entropy variation of the reaction can be found (eq.26):

$$T^* = \frac{\Delta_r H}{\Delta_r S} \quad (26)$$

For many systems, therefore, determining both enthalpy and reaction entropy from the respective formation parameters is sufficient to estimate T*. However, for newly systems, one or more formation parameters could not be known and this approach cannot be made directly. Regarding the hydrates of tricalcium aluminate, $Ca_3Al_2O_6{\cdot}6H_2O$ is certainly a widely studied chemical specie due to its relevancy in ceramic and cement technologies, on the other hand, for $Ca_3Al_2O_6{\cdot}1.5H_2O$ it is difficult to find previously determined thermodynamic data. Table 14 below shows the standard thermodynamic parameters available in literature from previous studies.

Table 14. Thermodynamic parameters currently available in literature [66,75,76].

Specie	$\Delta_f G°$ (kJ/mol)	$\Delta_f H°$ (kJ/mol)	S° (J/mol K)
$Ca_3Al_2O_6{\cdot}6H_2O_{(s)}$	-5016.4	-5549.6	395.9
$Ca_3Al_2O_6{\cdot}1.5H_2O_{(s)}$	N/A	N/A	N/A

The approach, used for the determination of the reaction turning temperature, therefore, was the use of an extrapolative method regarding its correlation with the

onset temperature measured by thermogravimetric analysis. As a matter of fact, as described by the German Society for Thermal Analysis (GEFTA), the linear correlation between the scanning rate β (K/min) and the corresponding T_{onset} allows with good accuracy to extrapolate T* at scan rate of zero [77]. Figure 29 shows the correlation between T_{onset} and β, for measurements at scanning rate 1, 2.5, 5, 10 and 20 K/min.

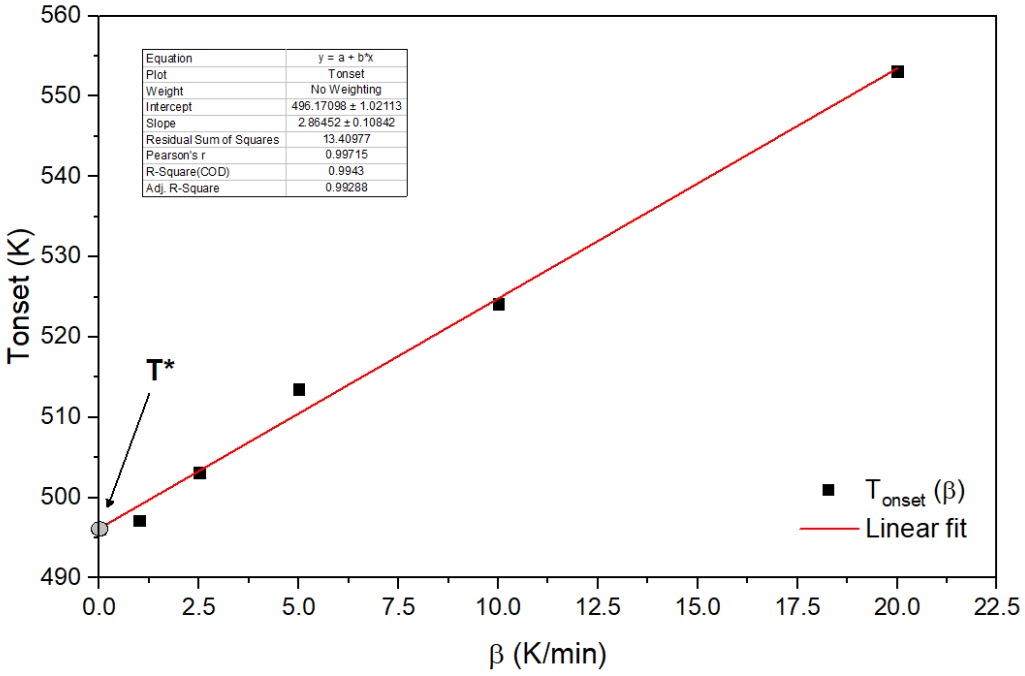

Figure 29. Onset temperature vs scanning rate for the determination of turning temperature

All measurements were performed with a quantity of material between 5.0-6.0 mg, previously dried, and under controlled flow of inert gas (Ar, 100mL/min). The onset temperatures, determined by the intersection between the straight sections before and after the beginning of the dehydration reaction, plotted as a function of β, gave T* as the intercept. It should be noted how the correlation coefficient obtained from the fitting is $R^2 = 0.993$. The extrapolation provided a value of T* = 496.2 K (223.05 °C) and gives important information on the operating temperature of the tricalcium aluminate hexahydrate/sesquihydrate pair, as for T < T* the equilibrium is shifted towards the reactants (hydration reaction), while for T > T* the equilibrium is shifted towards the products (dehydration reaction).

Based on what was stated earlier, regarding the lack of thermodynamic data on the formation of tricalcium aluminate sesqui-hydrate, the reaction enthalpy variation was also determined experimentally through differential scanning calorimetry (DSC), which is the most suitable technique for quantifying the involved heat, during a thermal process that occurs when the material is subjected to an increase of temperature. The DSC result on the investigated material was already showed in the previous section and was $\Delta_r H$ = 309.6 kJ/mol, considering purity of the material (98.6%) and molecular weight (378.3 g/mol). Per volume unit, this value would be 818.5 kJ/kg and 2.24 GJ/m^3, being the measured structural density 2.74 kg/dm^3. Figure 30 below compares the working couple (red dot) with the most common TCMs currently studied and which operate through a similar process involving the formation of covalent bonds (therefore, materials such as hydrate salts are excluded).

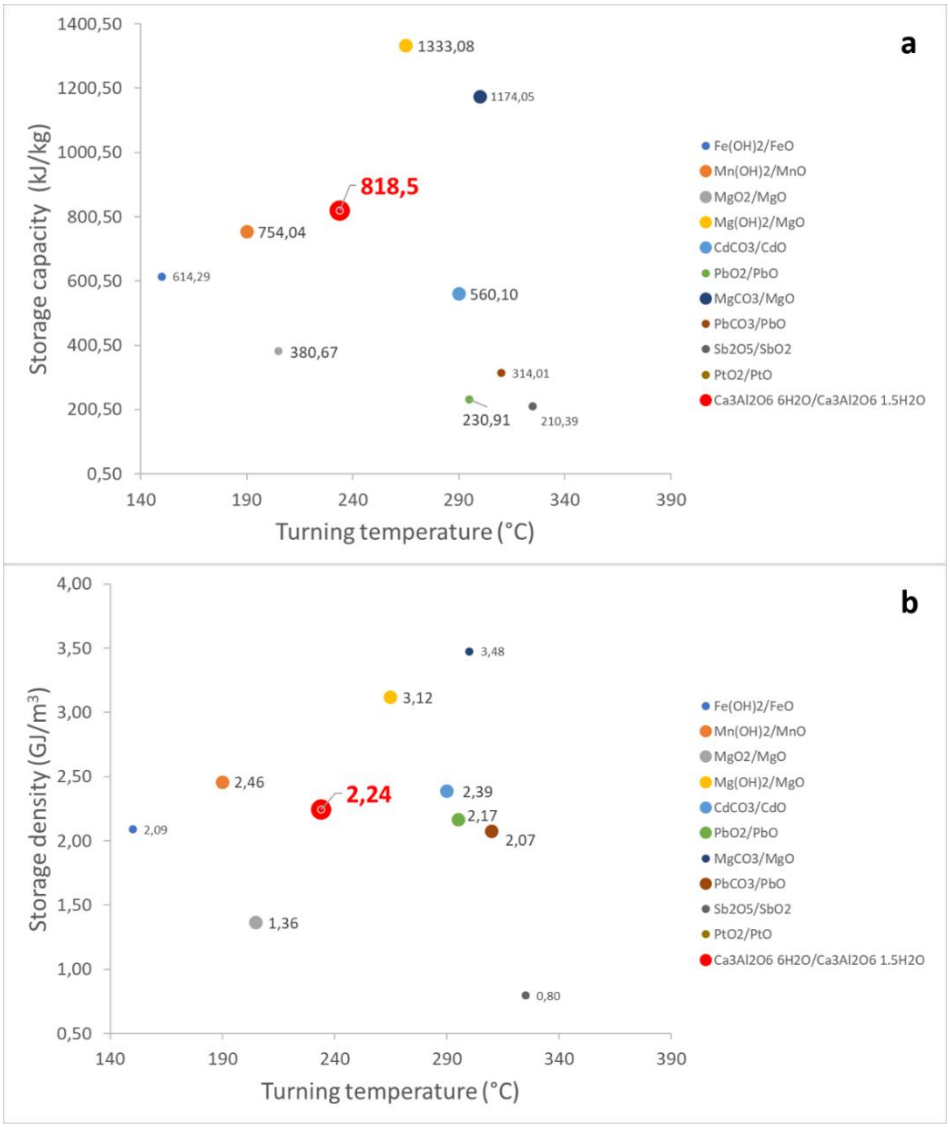

Figure 30. Comparison between $Ca_3Al_2O_6 \cdot 6H_2O/Ca_3Al_2O_6 \cdot 1.5H_2O$ and the most common medium-range TCMs.

The data shown in the graph for the compared couples are well known and readily available in the literature [63,78–81]. In the first image (a), the comparison is based on the theoretical storage capacity per mass unit. It can be seen that in the area where the $Ca_3Al_2O_6 \cdot 6H_2O/Ca_3Al_2O_6 \cdot 1.5H_2O$ pair stands with 818.4 kJ/kg there is a local empty space. Furthermore, it can be observed that the material has a theoretical storage capacity greater than many of the proposed materials (the nearest is $Mn(OH)_2/MnO$ whit 754.04 kJ/kg), and only $Mg(OH)_2/MgO$ (1333.08 kJ/kg) and $Mg(CO_3)_2/MgO$ (1174.05 kJ/kg) are more promising. In addition, a further advantage lies in the chemical composition, where certainly the use of metals such as calcium and aluminum is more beneficial from an economic and

also environmental point of view, compared to metals such as Mn, Cd, Pb, Sb and Pt. In the second image (b), the comparison is based on the theoretical storage density (or storage capacity per volume unit). Also in this second image we see an area around the pair based on tricalcium aluminate in which there are not many alternatives, however, in this case the system presents a storage density (2.24 GJ/m^3) slightly minor than $Mn(OH)_2$/MnO and $CdCO_3$/CdO pairs (2.46 GJ/m^3 and 2.49 GJ/m^3, respectively), beyond the two aforementioned $Mg(OH)_2$/MgO (3.12 GJ/m^3) and $Mg(CO_3)_2$/MgO (3.48 GJ/m^3). However, the studied material can be considered as a valid competitor in this field of materials. Of course, the one presented in this paragraph is only a preliminary consideration based on few data. Since this is a branch of research on tricalcium aluminate hexahydrate still under development, further and more comprehensive comparisons will be proposed in subsequent works. Despite this, the data obtained are encouraging in bringing forward new ideas regarding this material and its application.

3.4.2 Kinetic evaluation of the working pair

Knowing the thermodynamics of a TCM is important to suitably place it in an energy storage system operating in the suitable conditions. However, on the accomplishment of a suitable reactor, the reaction kinetic plays a fundamental role. Therefore, the development of kinetic models that better describe the dehydration and hydration reactions is equally important in the development of a new energy storage system. Under this consideration, a kinetic study parallel to the thermodynamic one is currently underway. The modeling has, as its ultimate goal, to develop a kinetic control equation for dehydration (equation 27) and hydration (equation 28) processes, in the form:

$$\frac{d\alpha}{dT} = \left(\frac{A}{\beta}\right) exp\left(-\frac{E}{RT}\right) f(\alpha_d) \quad (27)$$

$$\frac{d\alpha}{dt} = A\ exp\left(-\frac{E}{RT}\right) h(p) f(\alpha_h) \quad (28)$$

Where A is the pre-exponential factor, β is the heating rate, E is the apparent activation energy, h(p) is the pressure-dependence term and f(α) is the model that

describes the reaction mechanism. The reaction rate is expressed in dependence on the temperature in eq. 27 since the study of the decomposition reactions is difficult to carry out in isothermal conditions. What is more common, actually, is that the reaction begins during heating, for this reason it is preferred to determine the kinetic parameters through non-isothermal conditions with constant heating rates. The hydration reaction kinetic, on the other hand, can be easily studied in isothermal conditions, the desired temperature can be reached while the sample is in inert atmosphere and subsequently the water vapor is supplied. Under these conditions, it becomes meaningful to consider the pressure dependence term, being p_{H2O} an important parameter that manages the hydration reaction. As said before, the term f(α) is a typical model that describes the shape of α, which is the extent of conversion, calculated according to the Equations 29-30 for dehydration (α_d) and hydration (α_h) reactions. Where the subscripts "i" and "f" refer to the mass at the beginning and at the end of the reaction, while "t" indicates the mass at a given time during the reaction. The extent of conversion is then the normalized mass by the max weight, it follows that α has values in the range from 0 to 1.

Dehydration reaction

$$\alpha_d = \frac{m_i - m_t}{m_i - m_f} \qquad (29)$$

Hydration reaction

$$\alpha_h = \frac{m_t - m_i}{m_f - m_i} \qquad (30)$$

- *Dehydration kinetic*

The following are the preliminary results on the study of the dehydration kinetics of the material. The experimental part concerning the dehydration kinetics consists in the thermogravimetric analysis at different scan rates (β), 1, 2.5, 5 and 7.5 K/min (currently). The measurements are performed in platinum crucibles, using a sample quantity between 7 and 9 mg. The method consists of an isotherm at 125 ° C for

1h, followed by a temperature ramp up to 500 °C. The data processing is made by means of the NETZSCH Kinetics Neo software.

The first approach to the kinetic study concerned the determination of the activation energy parameter (E, kJ/mol) and pre-exponential factor (A, min^{-1}), through the application of the isoconversional method. This method is based on the idea that, at constant α, the reaction rate is exclusively dependent on the temperature. Under this assumption, the correlation between α, reached at a given scanning rate β, and the temperature T at which this conversion value is achieved, is the following (Friedman method, eq. 31:

$$\ln\left[\left(\frac{d\alpha}{dt}\right)\right]_{\alpha,i} = \ln[f(\alpha)A_\alpha] - \frac{E_\alpha}{RT_{\alpha,i}} \qquad (31)$$

Therefore, by plotting the term to the left-hand side as a function of 1/T, a linear relationship is obtained. Then, from slope and intercept it is possible to derive E and A (Figure 30).

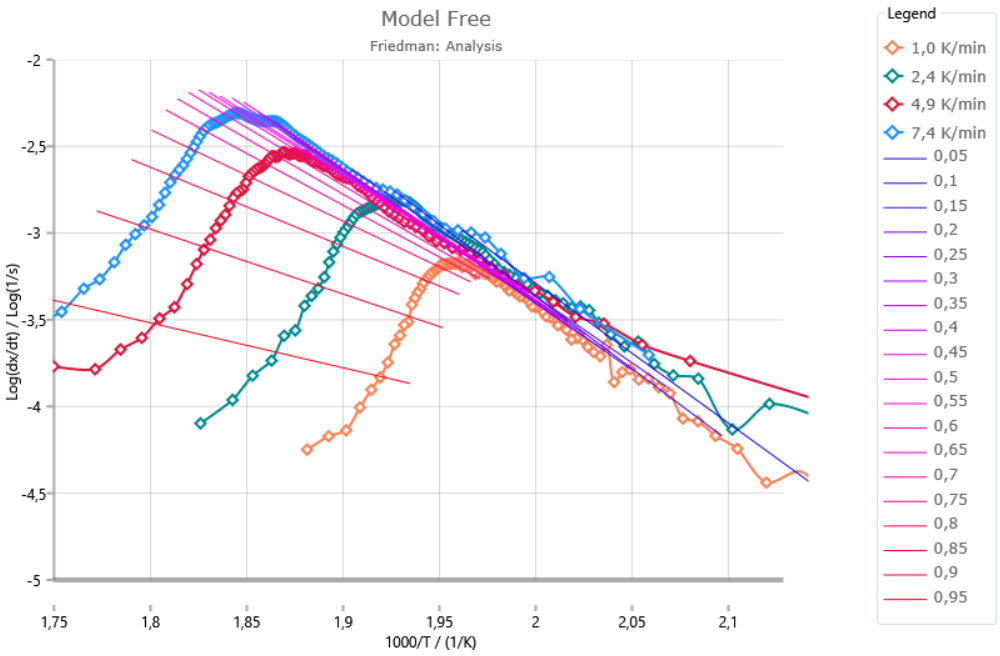

Figure 30. Isoconversional Friedman method application to tricalcium aluminate hexahydrate dehydration kinetic.

The image shows the linear relationships obtained by plotting the experimental data got from the temperature ramps, at different values of α (Δ = 0.05). In the ideal case, all the straight lines should show the same slope, thus leading to

constant values of E and A. What can be observed, also depending on the quality of the data, is that the two parameters are a function of α. In these cases, two alternatives are possible:

- E and A have a decreasing trend: usually the reaction kinetics is simple and the method is valid for determining an average value of the two parameters.

- E and A do not show a precise trend, the kinetics of the reaction are complex (i.e. multistep) and the method must be applied by splitting the experimental data.

Evaluated a simple kinetic for the system (Figure 31), the average values for activation energy and pre-exponential factor have been calculated, considering the whole range of α 0.05-0.95:

- E = 140.2 ± 13.12 kJ/mol
- Log(A) = 11.508 ± 1.327

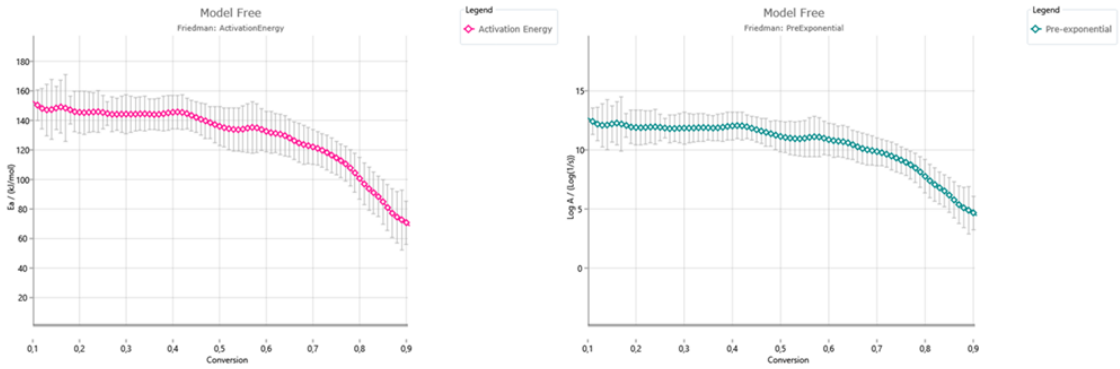

Figure 31. Dependence of E and A on the degree of conversion α.

The second approach was to apply a kinetic model to the experimental data (model-based). To do this, a descriptive model of order n (Fn) was selected and a fitting was developed on the curves, inserting as basic parameters the values of E and A obtained from the isoconversional method. In this way, the elaborated model has led to a fitting with R^2 = 0.9985, if the range of α up to 0.90 is considered. The parameters obtained applying a model Fn are E = 147.13 and Log (A) = 12.12. As can also be seen in Figure 32, in the last section of the curves (α > 0.9), the model and experimental data are particularly divergent. This means that additional data are still required to improve the modeling.

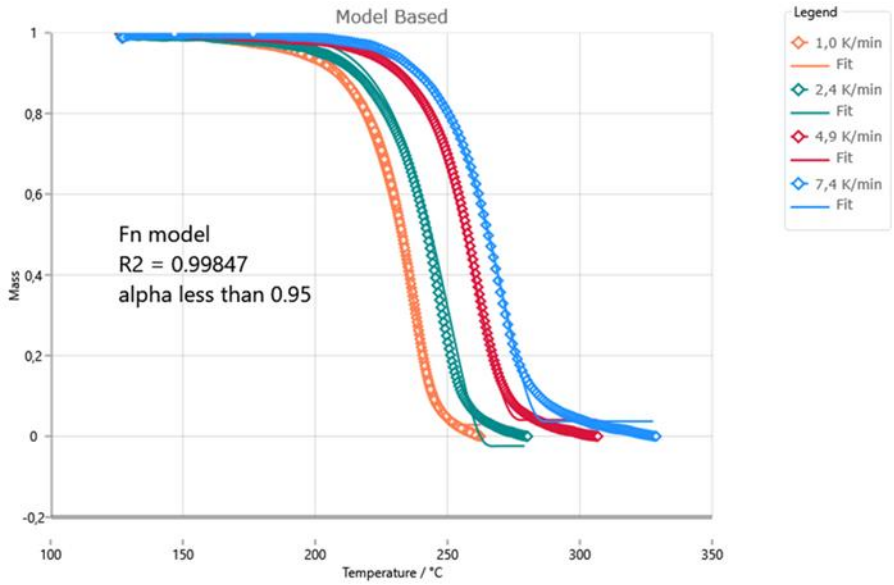

Figure 32. Experimental (straight lines) and model (points) comparison for model-based method.

4. CONCLUSIONS AND FUTURE REMARKS

The aim of this PhD thesis was to develop new materials for thermochemical storage. As discussed, different methods were studied and compared as possible strategies to obtain low-cost tricalcium aluminate hexahydrate materials. The solid-solid reaction showed that it is not possible to obtain a material with appropriate thermochemical properties without going through a preliminary synthetic route leading to an improved chemical interaction between Ca^{2+} and Al^{3+}. On the other hand, only co-precipitation did not lead to the desired material. A good approach was then the PCH method.

Regarding the structural and thermochemical characterization, a higher katoite content (98.6%) is obtained if a 1:1 Ca/Al ratio is initially used, which also results in a higher heat of dehydration (807.0 kJ/kg), compared to the other products.

Considering the dehydration/hydration behavior, the samples have a structural change during the cycles under the applied conditions. As a result, a decrease in conversion efficiencies, and hence released heat, is observed compared to the starting materials. For these reasons, calcium hydroxide seems to be important on the stabilization of the material, partially preventing the decomposition phenomena.

Indeed, once cycle stability is achieved, the amount of heat stored/released per unit mass is similar for both PCH products (about 260 kJ/kg of hydrated material), while in terms of storage density, CA-11 shows the highest capacity (224.2 MJ/m^3). Further consideration on cycling demonstrated how the efficiency of conversion for the material is influenced by the system in which it operates (at clearly higher H_2O pressures, hydration yield is still ~90% at the fifth cycle.

A thermodynamic/kinetics study to better understand the system and, at the same time, improve it, is currently going forward and some interesting results have been already obtained.

In future development, further studies will be conducted to improve the material, considering different preparation methods, to obtain more performing composite systems, and more suitable instrumental setups. Long-term cyclic stability will be evaluated in order to make this low-cost, non-toxic material a worthy competitor to current thermochemical energy storage systems.

5. REFERENCES

1. European Union *Statistical Pocketbook 2019: EU energy*; 2019; ISBN 9789276088196.

2. https://www.iea.org/ INTERNATIONAL ENERGY AGENCY: Origins and Structure. *Int. Energy Agency* 1994, *1*, 428.

3. Weir, T. Renewable energy in the Pacific Islands: Its role and status. *Renew. Sustain. Energy Rev.* 2018, *94*, 762–771, doi:10.1016/j.rser.2018.05.069.

4. Iten, M.; Liu, S.; Shukla, A. A review on the air-PCM-TES application for free cooling and heating in the buildings. *Renew. Sustain. Energy Rev.* 2016, *61*, 175–186, doi:10.1016/j.rser.2016.03.007.

5. Sarbu, I.; Sebarchievici, C. Solar Heating and Cooling for a Sustainable Energy Future in Europe(Vision Potential Deployment Roadmap Strategic Research Agenda). *Eur. Renew. Energy Centres Agency (EUREC Agency)* 2018, 65–76.

6. Dincer, I.; Rosen, M.A.; Ahmadi, P. Optimization of energy systems. *Optim. Energy Syst.* 2017, 1–453, doi:10.1002/9781118894484.

7. Medrano, M.; Yilmaz, M.O.; Nogués, M.; Martorell, I.; Roca, J.; Cabeza, L.F. Experimental evaluation of commercial heat exchangers for use as PCM thermal storage systems. *Appl. Energy* 2009, *86*, 2047–2055, doi:10.1016/j.apenergy.2009.01.014.

8. Noro, M.; Lazzarin, R.M.; Busato, F. Solar cooling and heating plants: An energy and economic analysis of liquid sensible vs phase change material (PCM) heat storage. *Int. J. Refrig.* 2014, *39*, 104–116, doi:10.1016/j.ijrefrig.2013.07.022.

9. Khan, M.M.A.; Saidur, R.; Al-Sulaiman, F.A. A review for phase change materials (PCMs) in solar absorption refrigeration systems. *Renew. Sustain. Energy Rev.* 2017, *76*, 105–137, doi:10.1016/j.rser.2017.03.070.

10. Chidambaram, L.A.; Ramana, A.S.; Kamaraj, G.; Velraj, R. Review of solar cooling methods and thermal storage options. *Renew. Sustain. Energy Rev.* 2011, *15*, 3220–3228, doi:10.1016/j.rser.2011.04.018.

11. Zhai, X.Q.; Wang, X.L.; Wang, T.; Wang, R.Z. A review on phase change cold

storage in air-conditioning system: Materials and applications. *Renew. Sustain. Energy Rev.* 2013, *22*, 108–120, doi:10.1016/j.rser.2013.02.013.

12. Liu, M.; Saman, W.; Bruno, F. Review on storage materials and thermal performance enhancement techniques for high temperature phase change thermal storage systems. *Renew. Sustain. Energy Rev.* 2012, *16*, 2118–2132, doi:10.1016/j.rser.2012.01.020.

13. Moreno, P.; Solé, C.; Castell, A.; Cabeza, L.F. The use of phase change materials in domestic heat pump and air-conditioning systems for short term storage: A review. *Renew. Sustain. Energy Rev.* 2014, *39*, 1–13, doi:10.1016/j.rser.2014.07.062.

14. Zhou, D.; Zhao, C.Y.; Tian, Y. Review on thermal energy storage with phase change materials (PCMs) in building applications. *Appl. Energy* 2012, *92*, 593–605, doi:10.1016/j.apenergy.2011.08.025.

15. Sharma, A.; Tyagi, V. V.; Chen, C.R.; Buddhi, D. Review on thermal energy storage with phase change materials and applications. *Renew. Sustain. Energy Rev.* 2009, *13*, 318–345, doi:10.1016/j.rser.2007.10.005.

16. Pintaldi, S.; Perfumo, C.; Sethuvenkatraman, S.; White, S.; Rosengarten, G. A review of thermal energy storage technologies and control approaches for solar cooling. *Renew. Sustain. Energy Rev.* 2015, *41*, 975–995, doi:10.1016/j.rser.2014.08.062.

17. Tian, Y.; Zhao, C.Y. A review of solar collectors and thermal energy storage in solar thermal applications. *Appl. Energy* 2013, *104*, 538–553, doi:10.1016/j.apenergy.2012.11.051.

18. Oró, E.; de Gracia, A.; Castell, A.; Farid, M.M.; Cabeza, L.F. Review on phase change materials (PCMs) for cold thermal energy storage applications. *Appl. Energy* 2012, *99*, 513–533, doi:10.1016/j.apenergy.2012.03.058.

19. Sarkar, J.; Bhattacharyya, S. Application of graphene and graphene-based materials in clean energy-related devices Minghui. *Arch. Thermodyn.* 2012, *33*, 23–40, doi:10.1002/er.

20. Al-Abidi, A.A.; Bin Mat, S.; Sopian, K.; Sulaiman, M.Y.; Mohammed, A.T. CFD

applications for latent heat thermal energy storage: A review. *Renew. Sustain. Energy Rev.* 2013, *20*, 353–363, doi:10.1016/j.rser.2012.11.079.

21. IRENA; IEA-ETSAP Technology Brief - Electricity Storage. 2012, 28.

22. Hauer, A. Storage Technology Issues and Opportunities, International Low-Carbon Energy Technology Platform. In Proceedings of the Strategic and Cross-Cutting Workshop "Energy Storage—Issues and Opportunities", Paris, France, 15 February 2011. 2011.

23. De Gracia, A.; Cabeza, L.F. Phase change materials and thermal energy storage for buildings. *Energy Build.* 2015, *103*, 414–419, doi:10.1016/j.enbuild.2015.06.007.

24. Kumar, A.; Shukla, S.K. A Review on Thermal Energy Storage Unit for Solar Thermal Power Plant Application. *Energy Procedia* 2015, *74*, 462–469, doi:10.1016/j.egypro.2015.07.728.

25. Heier, J.; Bales, C.; Martin, V. Combining thermal energy storage with buildings - A review. *Renew. Sustain. Energy Rev.* 2015, *42*, 1305–1325, doi:10.1016/j.rser.2014.11.031.

26. Kenisarin, M.; Mahkamov, K. Passive thermal control in residential buildings using phase change materials. *Renew. Sustain. Energy Rev.* 2016, *55*, 371–398, doi:10.1016/j.rser.2015.10.128.

27. Basecq, V.; Michaux, G.; Inard, C.; Blondeau, P. Short-term storage systems of thermal energy for buildings: a review. *Adv. Build. Energy Res.* 2013, *7*, 66–119, doi:10.1080/17512549.2013.809271.

28. Santos, T.; Kolokotroni, M.; Hopper, N.; Yearley, K. Experimental study on the performance of a new encapsulation panel for PCM's to be used in the PCM-Air heat exchanger. *Energy Procedia* 2019, *161*, 352–359, doi:10.1016/j.egypro.2019.02.105.

29. Wang, Z.; Liu, S.; Ma, G.; Xie, S.; Du, G.; Sun, J.; Jia, Y. Preparation and properties of caprylic-nonanoic acid mixture/expanded graphite composite as phase change material for thermal energy storage. *Int. J. Energy Res.* 2017, *41*, 2555–2564, doi:10.1002/er.3830.

30. Regin, A.F.; Solanki, S.C.; Saini, J.S. Heat transfer characteristics of thermal energy storage system using PCM capsules: A review. *Renew. Sustain. Energy Rev.* 2008, *12*, 2438–2458, doi:10.1016/j.rser.2007.06.009.

31. Cabeza, L.F.; Castell, A.; Barreneche, C.; De Gracia, A.; Fernández, A.I. Materials used as PCM in thermal energy storage in buildings: A review. *Renew. Sustain. Energy Rev.* 2011, *15*, 1675–1695, doi:10.1016/j.rser.2010.11.018.

32. Amaral, C.; Vicente, R.; Marques, P.A.A.P.; Barros-Timmons, A. Phase change materials and carbon nanostructures for thermal energy storage: A literature review. *Renew. Sustain. Energy Rev.* 2017, *79*, 1212–1228, doi:10.1016/j.rser.2017.05.093.

33. Liu, L.; Alva, G.; Huang, X.; Fang, G. Preparation, heat transfer and flow properties of microencapsulated phase change materials for thermal energy storage. *Renew. Sustain. Energy Rev.* 2016, *66*, 399–414, doi:10.1016/j.rser.2016.08.035.

34. Rigotti, D.; Dorigato, A.; Pegoretti, A. 3D printable thermoplastic polyurethane blends with thermal energy storage/release capabilities. *Mater. Today Commun.* 2018, *15*, 228–235, doi:10.1016/j.mtcomm.2018.03.009.

35. Nomura, T.; Okinaka, N.; Akiyama, T. Impregnation of porous material with phase change material for thermal energy storage. *Mater. Chem. Phys.* 2009, *115*, 846–850, doi:10.1016/j.matchemphys.2009.02.045.

36. Tyagi, V. V.; Kaushik, S.C.; Tyagi, S.K.; Akiyama, T. Development of phase change materials based microencapsulated technology for buildings: A review. *Renew. Sustain. Energy Rev.* 2011, *15*, 1373–1391, doi:10.1016/j.rser.2010.10.006.

37. Delgado, M.; Lázaro, A.; Mazo, J.; Zalba, B. Review on phase change material emulsions and microencapsulated phase change material slurries: Materials, heat transfer studies and applications. *Renew. Sustain. Energy Rev.* 2012, *16*, 253–273, doi:10.1016/j.rser.2011.07.152.

38. Fay, D.L. *Differential Scanning Calorimetry.*; 1967; ISBN 9783642055935.

39. Li, G.; Hwang, Y.; Radermacher, R. Review of cold storage materials for air

conditioning application. *Int. J. Refrig.* 2012, *35*, 2053–2077, doi:10.1016/j.ijrefrig.2012.06.003.

40. Kerskes, H.; Mette, B.; Bertsch, F.; Asenbeck, S.; Drück, H. Chemical energy storage using reversible solid/gas-reactions (CWS) - Results of the research project. *Energy Procedia* 2012, *30*, 294–304, doi:10.1016/j.egypro.2012.11.035.

41. Fujii, I.; Tsuchiya, K.; Higano, M.; Yamada, J. Studies of an energy storage system by use of the reversible chemical reaction: CaO + H2O ⇌ Ca(OH)2. *Sol. Energy* 1985, *34*, 367–377, doi:10.1016/0038-092X(85)90049-0.

42. Garg, H.P..; Mullick, S.C..; Bhargava, A.K. *Solar Thermal Energy Storage*; 1985; ISBN 9789401088411.

43. Paksoy, H.Ö. Part ii. climate change and thermal energy storage.

44. Guy, E. Solar Heat Storage Using Chemical Reactions. *J. Solid State Chem.* 1977, *22*, 51–61.

45. Kato, Y.; Yamashita, N.; Kobayashi, K.; Yoshizawa, Y. Kinetic study of the hydration of magnesium oxide for a chemical heat pump. *Appl. Therm. Eng.* 1996, *16*, 853–862, doi:10.1016/1359-4311(96)00009-9.

46. Kato, Y.; Sasaki, Y.; Yoshizawa, Y. Packed bed reactor demonstration of magnesium oxide/water chemical heat pump. *J. Chem. Eng. Japan* 2003, *36*, 833–839.

47. Kato, Y.; Kobayashi, K.; Yoshizawa, Y. Durability to repetitive reaction of magnesium oxide/water reaction system for a heat pump. *Appl. Therm. Eng.* 1998, *18*, 85–92, doi:10.1016/s1359-4311(97)00058-6.

48. Yim, T.; Kim, H.S.; Lee, J.Y. Cyclic assessment of magnesium oxide with additives as a thermochemical material to improve the mechanical strength and chemical reaction. *Energies* 2018, *11*, doi:10.3390/en11092366.

49. Kato, Y.; Saito, T.; Soga, T.; Ryu, J.; Yoshizawa, Y. Durable reaction material development for magnesium oxide/water chemical heat pump. *J. Chem. Eng. Japan* 2007, *40*, 1264–1269, doi:10.1252/jcej.07WE218.

50. Kato, Y.; Sasaki, Y.; Yoshizawa, Y. Magnesium oxide/water chemical heat pump to enhance energy utilization of a cogeneration system. *Energy* 2005, *30*, 2144–

2155, doi:10.1016/j.energy.2004.08.019.

51. Kato, Y.; Takahashi, R.; Sekiguchi, T.; Ryu, J. Study on medium-temperature chemical heat storage using mixed hydroxides. *Int. J. Refrig.* 2009, *32*, 661–666, doi:10.1016/j.ijrefrig.2009.01.032.

52. Ryu, J.; Takahashi, R.; Hirao, N.; Kato, Y. Effect of transition metal mixing on reactivities of magnesium oxide for chemical heat pump. *J. Chem. Eng. Japan* 2007, *40*, 1281–1286, doi:10.1252/jcej.07WE171.

53. Tae Kim, S.; Ryu, J.; Kato, Y. Reactivity enhancement of chemical materials used in packed bed reactor of chemical heat pump. *Prog. Nucl. Energy* 2011, *53*, 1027–1033, doi:10.1016/j.pnucene.2011.05.013.

54. Mastronardo, E.; Bonaccorsi, L.; Kato, Y.; Piperopoulos, E.; Lanza, M.; Milone, C. Strategies for the enhancement of heat storage materials performances for MgO/H2O/Mg(OH)2 thermochemical storage system. *Appl. Therm. Eng.* 2017, *120*, 626–634, doi:10.1016/j.applthermaleng.2017.04.004.

55. Mastronardo, E.; Kato, Y.; Bonaccorsi, L.; Piperopoulos, E.; Milone, C. Thermochemical storage of middle temperature wasted heat by functionalized C/Mg(OH)2 hybrid materials. *Energies* 2017, *10*, doi:10.3390/en10010070.

56. Mastronardo, E.; Bonaccorsi, L.; Kato, Y.; Piperopoulos, E.; Lanza, M.; Milone, C. Thermochemical performance of carbon nanotubes based hybrid materials for MgO/H2O/Mg(OH)2 chemical heat pumps. *Appl. Energy* 2016, *181*, 232–243, doi:10.1016/j.apenergy.2016.08.041.

57. Mastronardo, E.; Bonaccorsi, L.; Kato, Y.; Piperopoulos, E.; Milone, C. Efficiency improvement of heat storage materials for MgO/H2O/Mg(OH)2 chemical heat pumps. *Appl. Energy* 2016, *162*, 31–39, doi:10.1016/j.apenergy.2015.10.066.

58. Ogura, H.; Mujumdar, A.S. Proposal for a novel chemical heat pump dryer. *Dry. Technol.* 2000, *18*, 1033–1053, doi:10.1080/07373930008917752.

59. Ogura, H.; Ishida, H.; Yokooji, R.; Kage, H.; Matsuno, Y.; Mujumdar, A.S. Experimental studies on a novel chemical heat pump dryer using a gas-solid reaction. *Dry. Technol.* 2001, *19*, 1461–1477, doi:10.1081/DRT-100105300.

60. Kato, Y.; Saku, D.; Harada, N.; Yoshizawa, Y. Utilization of high temperature heat

from nuclear reactor using inorganic chemical heat pump. *Prog. Nucl. Energy* 1998, *32*, 563–570, doi:10.1016/s0149-1970(97)00044-9.

61. Kato, Y.; Harada, N.; Yoshizawa, Y. Kinetic feasibility of a chemical heat pump for heat utilization of high-temperature processes. *Appl. Therm. Eng.* 1999, *19*, 239–254, doi:10.1016/s1359-4311(98)00049-0.

62. Dipu, A.L.; Ryu, J.; Kato, Y. Carbon dioxide electrolysis for a carbon-recycling iron-making system. *ISIJ Int.* 2012, *52*, 1427–1432, doi:10.2355/isijinternational.52.1427.

63. Cabeza, L.F.; Solé, A.; Barreneche, C. Review on sorption materials and technologies for heat pumps and thermal energy storage. *Renew. Energy* 2017, *110*, 3–39, doi:10.1016/j.renene.2016.09.059.

64. Scrivener, K.L.; Cabiron, J.L.; Letourneux, R. High-performance concretes from calcium aluminate cements. *Cem. Concr. Res.* 1999, *29*, 1215–1223, doi:10.1016/S0008-8846(99)00103-9.

65. Geiger, C.A.; Dachs, E.; Benisek, A. Thermodynamic behavior and properties of katoite (hydrogrossular): A calorimetric study. 2012, doi:10.2138/am.2012.4106.

66. Stein, H.N. Thermodynamic considerations on the hydration mechanisms of Ca3SiO5 and Ca3Al2O6. *Cem. Concr. Res.* 1972, *2*, 167–177, doi:10.1016/0008-8846(72)90039-7.

67. Lacivita, V.; Mahmoud, A.; Arco, P.D.; Mustapha, S. Investigation of its Structural and Energetic Properties . *2*.

68. Cavenett The Dehydration of Tricalcium aluminate exahydrate. *J. Chem. Inf. Model.* 1941, *19*, 1689–1699, doi:10.1017/CBO9781107415324.004.

69. Ball, M.C.; Ladner, N.G.; Taylor, J.A. The dehydroxylation of tricalcium aluminate 6-hydrate. *Thermochim. Acta* 1976, *17*, 207–215, doi:10.1016/0040-6031(76)85027-7.

70. Rivas-Mercury, J.M.; Pena, P.; de Aza, A.H.; Turrillas, X. Dehydration of Ca3Al2(SiO4)y(OH)4(3−y) (0 < y < 0.176) studied by neutron thermodiffractometry J.M. *J. Eur. Ceram. Soc.* 2008, *28*, 1737–1748, doi:10.1016/j.jeurceramsoc.2007.12.038.

71. Callister, W.D.J.; Rethwisch, D.G. *Materials Science and Engineering*; Edises, 2017, 77-78, Ed.; ISBN 978-1-119-40549-8.

72. STAGNARO, P.; LUCIANO, G. and; UTZERI, R. Differential scanning calorimetry and thermogravimetric analysis in the thermal characterization of polymeric materials. 2021, 1–8.

73. Antonovič, V.; Keriene, J.; Boris, R.; Aleknevičius, M. The effect of temperature on the formation of the hydrated calcium aluminate cement structure. *Procedia Eng.* 2013, *57*, 99–106, doi:10.1016/j.proeng.2013.04.015.

74. Ukrainczyk, N.; Matusinović, T. Thermal properties of hydrating calcium aluminate cement pastes. *Cem. Concr. Res.* 2010, *40*, 128–136, doi:10.1016/j.cemconres.2009.09.005.

75. Torréns-Martín, D.; Fernández-Carrasco, L.; Martínez-Ramírez, S. Hydration of calcium aluminates and calcium sulfoaluminate studied by Raman spectroscopy. *Cem. Concr. Res.* 2013, *47*, 43–50, doi:10.1016/j.cemconres.2013.01.015.

76. SIMULTANEOUS ASSESSMENT OF THERMODYNAMIC FUNCTIONS OF CALCIUM ALUMINATES V . V . Kuzmenko , I . A . Uspenskaya , E . B . Rudnyi.

77. Wokon, M.; Block, T.; Nicolai, S.; Linder, M.; Schmücker, M. Thermodynamic and kinetic investigation of a technical grade manganese-iron binary oxide for thermochemical energy storage. *Sol. Energy* 2017, *153*, 471–485, doi:10.1016/j.solener.2017.05.045.

78. Cot-Gores, J.; Castell, A.; Cabeza, L.F. Thermochemical energy storage and conversion: A-state-of-the-art review of the experimental research under practical conditions. *Renew. Sustain. Energy Rev.* 2012, *16*, 5207–5224, doi:10.1016/j.rser.2012.04.007.

79. Cabeza, L.F. Thermal energy storage. *Compr. Renew. Energy* 2012, *3*, 211–253, doi:10.1016/B978-0-08-087872-0.00307-3.

80. Alva, G.; Lin, Y.; Fang, G. An overview of thermal energy storage systems. *Energy* 2018, *144*, 341–378, doi:10.1016/j.energy.2017.12.037.

81. Chan, C.W.; Ling-Chin, J.; Roskilly, A.P. A review of chemical heat pumps, thermodynamic cycles and thermal energy storage technologies for low grade heat

utilisation. *Appl. Therm. Eng.* 2013, *50*, 1257–1273, doi:10.1016/j.applthermaleng.2012.06.041.